

AWARD NUMBER: W81XWH-10-1-0739

TITLE: Voxel-Wise Time-Series Analysis of Quantitative MRI in Relapsing-Remitting MS: Dynamic Imaging Metrics of Disease Activity Including Pre-lesional Changes

PRINCIPAL INVESTIGATOR: Aaron Field

CONTRACTING ORGANIZATION: University of Wisconsin System
Madison, WI 53715

REPORT DATE: December 2015

TYPE OF REPORT: Final

PREPARED FOR: U.S. Army Medical Research and Materiel Command
Fort Detrick, Maryland 21702-5012

DISTRIBUTION STATEMENT: Approved for Public Release;
Distribution Unlimited

The views, opinions and/or findings contained in this report are those of the author(s) and should not be construed as an official Department of the Army position, policy or decision unless so designated by other documentation.

REPORT DOCUMENTATION PAGE				Form Approved OMB No. 0704-0188	
Public reporting burden for this collection of information is estimated to average 1 hour per response, including the time for reviewing instructions, searching existing data sources, gathering and maintaining the data needed, and completing and reviewing this collection of information. Send comments regarding this burden estimate or any other aspect of this collection of information, including suggestions for reducing this burden to Department of Defense, Washington Headquarters Services, Directorate for Information Operations and Reports (0704-0188), 1215 Jefferson Davis Highway, Suite 1204, Arlington, VA 22202-4302. Respondents should be aware that notwithstanding any other provision of law, no person shall be subject to any penalty for failing to comply with a collection of information if it does not display a currently valid OMB control number. PLEASE DO NOT RETURN YOUR FORM TO THE ABOVE ADDRESS.					
1. REPORT DATE December 2015		2. REPORT TYPE Final		3. DATES COVERED 30 Sept 2010 – 29 Sept 2015	
4. TITLE AND SUBTITLE Voxel-Wise Time-Series Analysis of Quantitative MRI in Relapsing-Remitting MS: Dynamic Imaging Metrics of Disease Activity Including Pre-Lesional Changes				5a. CONTRACT NUMBER W81XWH-10-1-0739	
				5b. GRANT NUMBER MS090152	
				5c. PROGRAM ELEMENT NUMBER	
6. AUTHOR(S) Aaron S. Field M.D., Ph.D. E-Mail: Afield@UWHealth.org				5d. PROJECT NUMBER	
				5e. TASK NUMBER	
				5f. WORK UNIT NUMBER	
7. PERFORMING ORGANIZATION NAME(S) AND ADDRESS(ES) University of Wisconsin- Madison Research and Sponsored Programs 21 N. Park St., Suite 6401 Madison, WI 53715-1218				8. PERFORMING ORGANIZATION REPORT NUMBER	
9. SPONSORING / MONITORING AGENCY NAME(S) AND ADDRESS(ES) U.S. Army Medical Research and Materiel Command Fort Detrick, Maryland 21702-5012				10. SPONSOR/MONITOR'S ACRONYM(S)	
				11. SPONSOR/MONITOR'S REPORT NUMBER(S)	
12. DISTRIBUTION / AVAILABILITY STATEMENT Approved for Public Release; Distribution Unlimited					
13. SUPPLEMENTARY NOTES					
14. ABSTRACT Previous MRI studies in MS have retrospectively analyzed normal-appearing brain tissue in locations where typical MS lesions ultimately appeared, finding pre-lesional changes in several MRI metrics. However, studies have not been entirely consistent and the development of a prototypical MS lesion cannot as yet be prospectively predicted. The primary objective of this project is to validate the "preactive" lesion hypothesis in MS by identifying the spatiotemporal imaging signature of white matter destined to undergo acute, focal inflammation and demyelination-specifically, one that will allow reliable, prospective detection of nascent lesions before they appear on conventional (non-quantitative) imaging. The specific aim is to acquire a longitudinal set of quantitative MRI metrics in MS patients and perform a multivariate spatiotemporal analysis of pre-lesional, normal-appearing white matter, seeking spatially clustered interval changes that presage the appearance of a typical MS plaque.					
15. SUBJECT TERMS Multiple Sclerosis, magnetic resonance imaging, longitudinal studies, preactive lesions					
16. SECURITY CLASSIFICATION OF:			17. LIMITATION OF ABSTRACT	18. NUMBER OF PAGES	19a. NAME OF RESPONSIBLE PERSON
a. REPORT	b. ABSTRACT	c. THIS PAGE			USAMRMC
U	U	U	UU	36	19b. TELEPHONE NUMBER (include area code)

Table of Contents

	<u>Page</u>
Introduction.....	4.
Body.....	4.
Key Research Accomplishments.....	8.
Reportable Outcomes.....	8.
Conclusion.....	9.
References.....	10.
Appendices.....	10.

I. INTRODUCTION:

Previous MRI studies in multiple sclerosis (MS) have retrospectively analyzed normal-appearing brain tissue in locations where typical MS lesions ultimately appeared, finding pre-lesional changes in several MRI metrics. However, studies have not been entirely consistent and the development of a prototypical MS lesion cannot as yet be prospectively predicted. The primary objective of this project is to validate the “preactive” lesion hypothesis in MS by identifying the spatiotemporal imaging signature of white matter (WM) destined to undergo acute, focal inflammation and demyelination—specifically, one that will allow reliable, prospective detection of nascent lesions before they appear on conventional (non-quantitative) imaging. The specific aim is to acquire a longitudinal set of quantitative MRI metrics in MS patients and perform a multivariate spatiotemporal analysis of pre-lesional, normal-appearing white matter, seeking spatially clustered interval changes that presage the appearance of a typical MS plaque.

II. BODY:

The key accomplishments achieved over the course of the project are detailed below, keyed to the tasks outlined in the Statement of Work.

II.A. Subject enrollment:

Recruitment for the study was challenging as several disease-modifying therapies were approved by the FDA and made available to patients during this phase of the study; this made it difficult to find subjects with active disease (necessary for new lesions to study) who were willing to forego therapy for the duration of the study (required by inclusion criteria). Seven treatment-naïve MS patients meeting inclusion criteria were ultimately enrolled and completed the eight monthly MRI scans. As it happened, the delay in enrollment may have been a “blessing in disguise” as it allowed us to continue the preparatory development and optimization of MRI acquisition methods, leading to several key accomplishments as detailed in the next section.

II.B. MRI acquisition:

We made several technical advances in quantitative MRI acquisition methods for the project, specifically in quantitative magnetization transfer (MT) imaging [1-7].

We developed a novel method for simultaneous calibration of excitation flip angle and MT saturation power [1-2]; accounting for B1 and flip angle variations is critical for longitudinal stability of MT imaging which, in turn, is required for the tracking of changes that occur in lesions over time. Previous studies relied on either B1 maps or flip angle maps, but not both, to correct both excitation flip and MT saturation power, which may result in significant errors in MT parameters. Our new method enabled the accounting for both sources of errors and, as a result, yielded more accurate MT measures (**Fig. 1**).

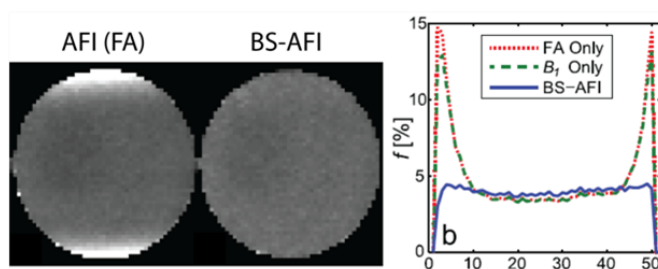


Figure 1. **Left:** Bound pool fraction f in a homogeneous gel phantom calculated using old MT method AFI (FA) and new method (BS-AFI). **Right:** Representative profiles through the images showing the old method overestimating the key MT measure in the areas close to the edges.

We also developed a new quantitative MT imaging method, modified cross-relaxation imaging, (mCRI) [5], which decreases the number of acquired images and scan time relative to existing methods while yielding more accurate (by ~16%) values of macromolecular proton fraction (MPF), an imaging biomarker of myelin content. This was achieved via novel modeling of MT exchange processes in steady-state sequences, an existing method that was transformed into a fast, minimum-acquisition protocol capable of mapping a subset of qMTI measures including MPF and $T1$ using only three MRI scans [6-7] (up to 60% reduction over state-of-the-art techniques). This advance was achieved by applying physiologically relevant constraints on the remaining model parameters and optimizing acquisition to minimize the impact of these parameters on accuracy. **Fig. 2** shows results of fast mCRI and illustrates the limitations of $R1=1/T1$ as an indirect measure of myelin. **Fig. 3** favorably compares MPF with an alternative MT-based myelin marker based on inhomogeneous MT effect (*ihMTR*). The final 7 min version of the protocol was applied in study subjects.

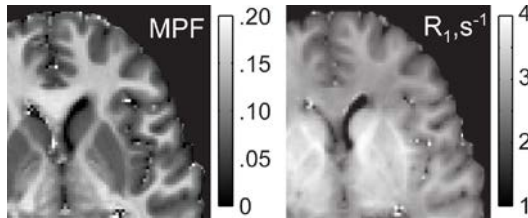


Figure 2. MPF and $R1=1/T1$ maps using our fast three-measurement mCRI with flip angle correction. Note excellent myelin contrast on MPF map.

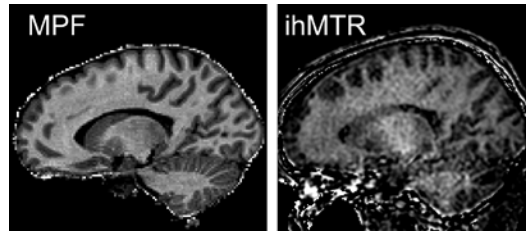


Figure 3. Comparison of MPF and *ihMTR* myelin-sensitive maps optimized to run in the same time (7 min; *ihMTR*: 1.9x1.9x3mm, 60 slices; MPF: 1.5 mm isotropic, 120 slices). Note much higher resolution/quality of MPF.

MPF imaging in WM is illustrated by **Fig. 5** below. Note that two different lesions appearing similar on standard T2-FLAIR images demonstrate different levels of tissue damage on MPF (green arrow – lesion with high residual myelination, red arrow – lesion with virtually no residual myelination). **Fig. 6** illustrates the promise of MPF to improve detection of focal GM pathology compared to conventional MRI and state-of-the-art double inversion recovery (DIR).

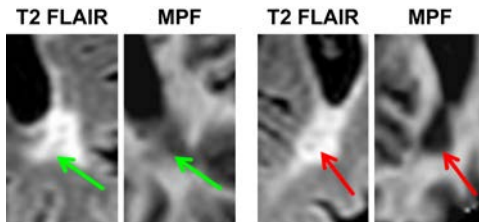


Figure 5. Two MS lesions appear similar on standard T2 FLAIR but different on MPF, presumably reflecting different levels of demyelination.

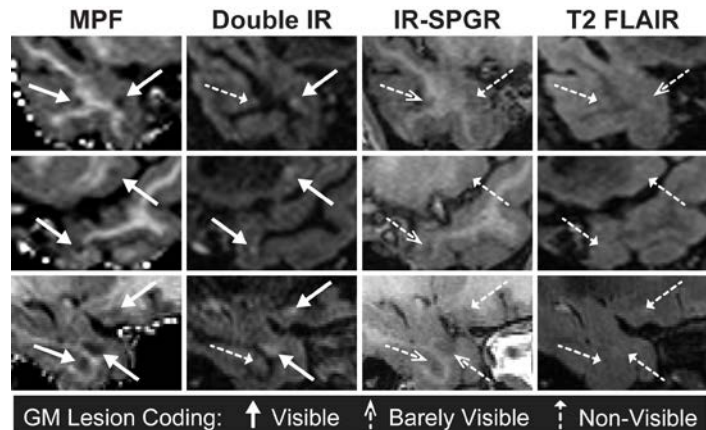


Figure 6. GM lesions on MPF, DIR (state-of-the-art GM imaging method in MS), and standard IR-SPGR and 3D T2 FLAIR. Note improved GM lesion depiction on MPF.

II.C. Image Processing:

We developed a semi-automated image processing pipeline for multiparametric images, with key stages including brain extraction, co-registration of images from different modalities and time-points, and segmentation of normal-appearing white matter (**Figs. 7-8**). All imaging data acquired in different orientations (axial and sagittal) were first converted to the NIFTI image format and their orientations changed to axial (orientation of the reference data). Skull stripping (brain extraction) was then performed on high-resolution 3D BRAVO T1-weighted images using the Brain Extraction Tool in the FSL software library (FMRIB, Oxford, UK). To correct intensity variations due to magnetic field inhomogeneity, non-uniformity correction was applied on the extracted brain BRAVO image using JIM analysis software (Xinapse Systems, UK). This reference BRAVO image was then co-registered to the MNI152 template (Montreal Neurological Institute) using the FLIRT (FMRIB Linear Image Registration Tool) brain image registration toolbox in FSL. Eddy current correction was applied to DTI data also using FSL software. All images for a given subject at all scan dates were co-registered to that subject's reference BRAVO series and the BRAVO brain mask generated in the first step was applied to all co-registered images. In addition, non-uniformity correction was applied to high-resolution 3D Cube T2-FLAIR images.

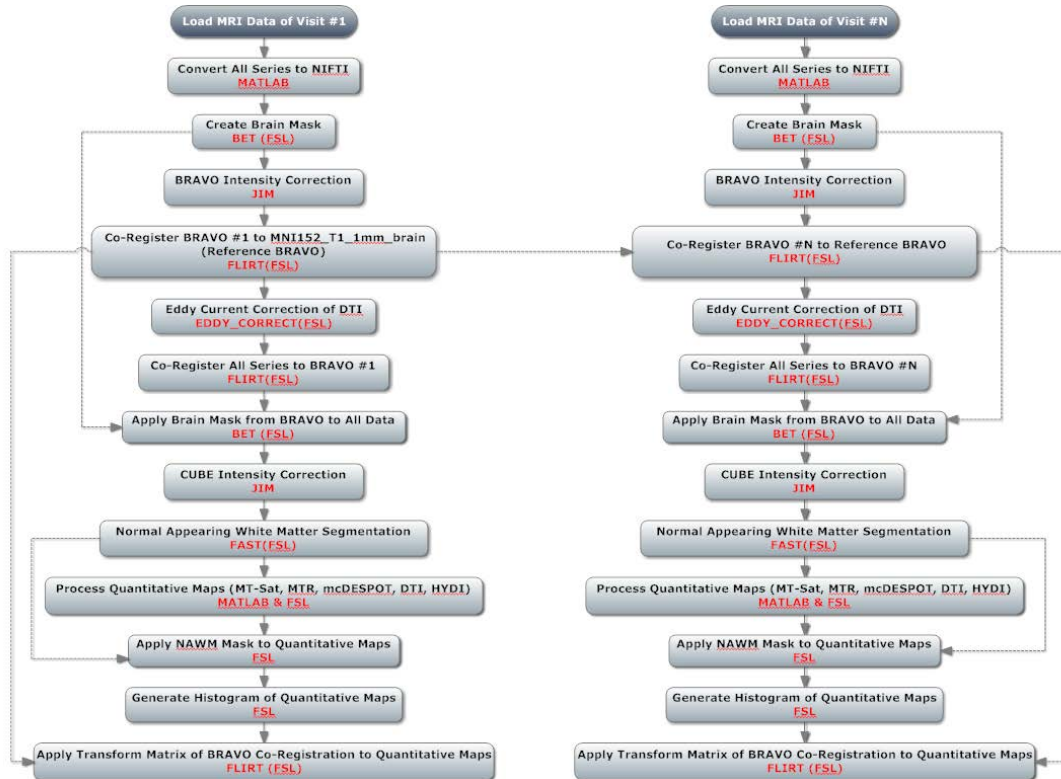


Figure 7: Overview of post-processing pipeline

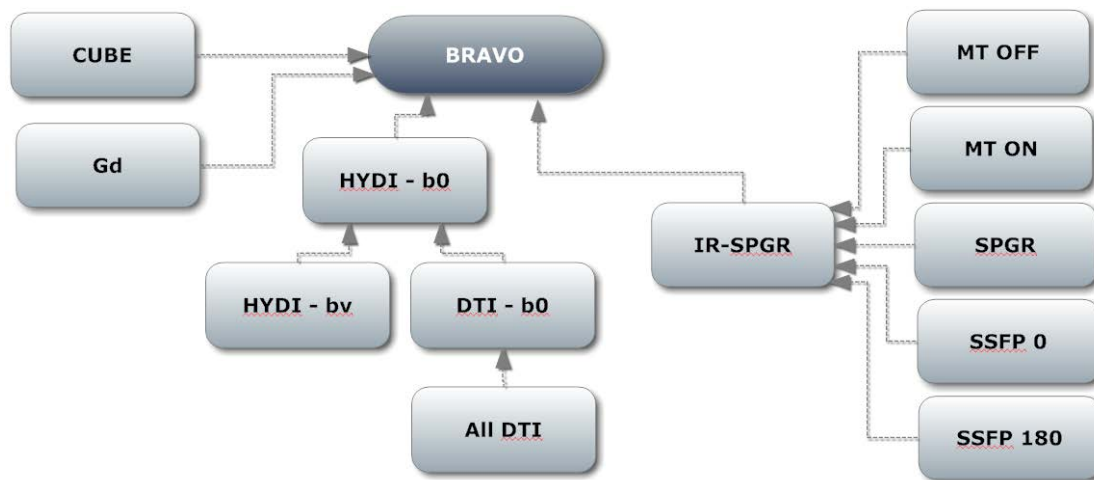


Figure 8: Block diagram of image co-registration steps to align quantitative (DTI, MT) with anatomical (T1, T2) images.

II.D. Data Analysis:

The image processing detailed above yielded a set of spatially and temporally co-registered, lesion-segmented, quantitative MRI maps that could be analyzed to identify any pre-lesional changes in MR parameters. An example is shown in **Fig. 9**. Lesions that appeared for the first time in any of the second-half MRI scans (i.e. with ≥ 4 pre-lesional scans available) were selected for analysis, seeking statistically significant differences in MRI parameters between the NAWM that evolved into a lesion versus the NAWM that did not.

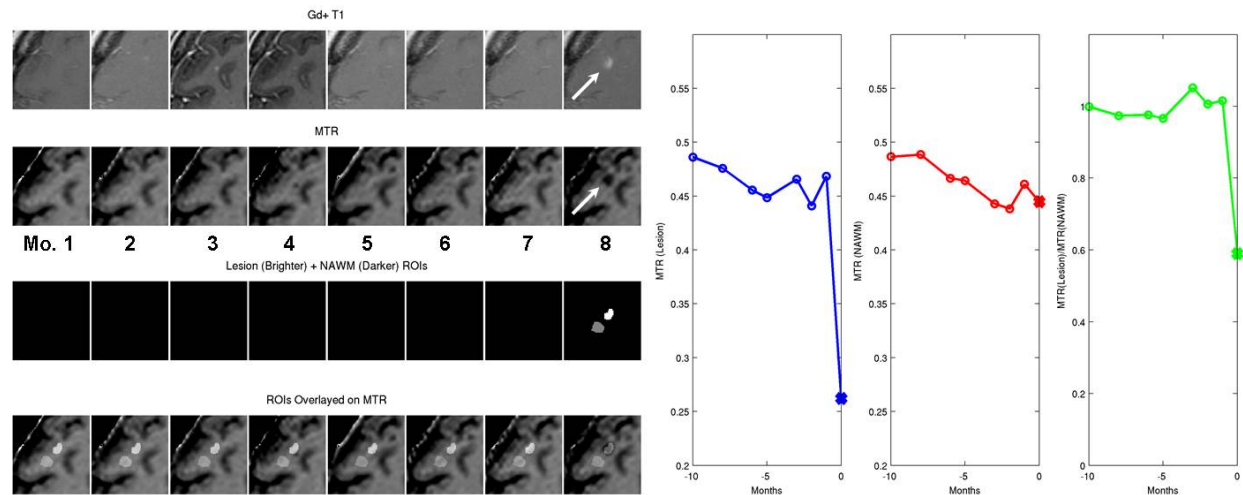


Figure 9. Serial monthly magnetization transfer ratio (MTR) maps spatiotemporally co-registered to post-contrast T1-weighted images (Gd+T1) for a subject who developed a new MS lesion in month #8 (arrows). Two regions of interest (ROIs), one encompassing the lesion and another normal-appearing white matter (NAWM), could then be tracked over the 7 monthly scans before the lesion appeared. Note that MTR in the lesion (blue) decreased precipitously relative to NAWM (red) when the lesion appeared but not before then (ratio of lesion to NAWM in green).

Analyzed parameters included four HYDI metrics: fractional anisotropy (FA), axial (Da) and radial (Dr) diffusivity and zero-displacement probability (Po), and four MT metrics: magnetization transfer ratio (MTR), MT saturation (MTSat), bound pool fraction (f) and

longitudinal relaxation rate (R1). There were no statistically significant differences between pre-lesional WM and other NAWM on any of the pre-lesional scans, for any of the parameters analyzed, that would have allowed the prediction of lesion appearance beforehand.

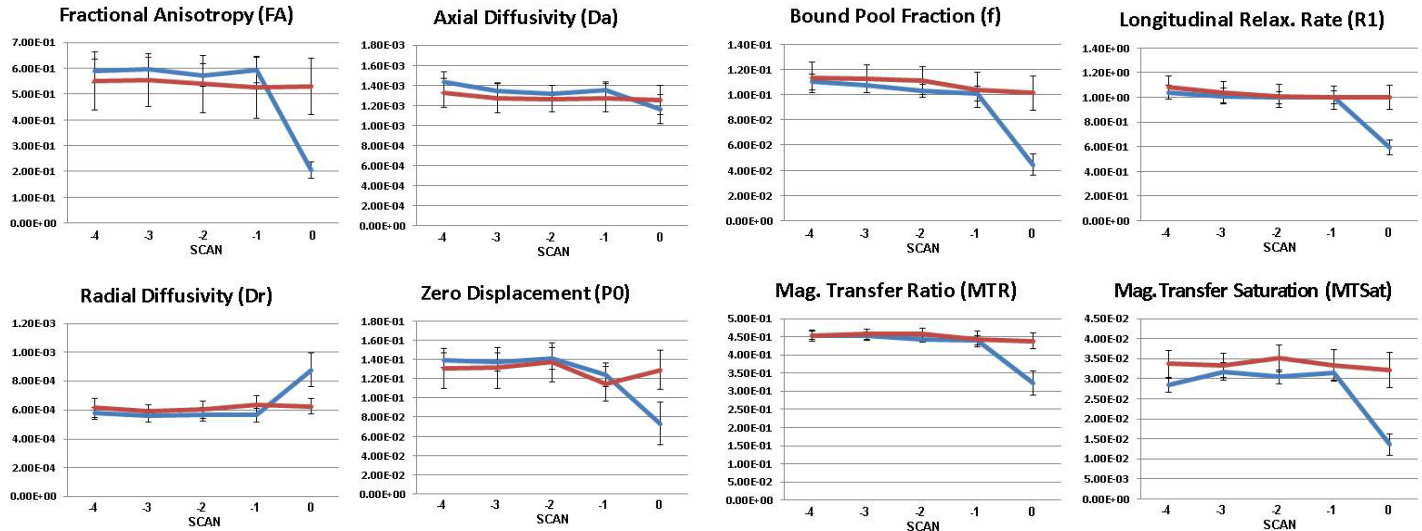


Figure 10. Summary of prelesional diffusion (HYDI) and magnetization transfer (MT) parameter tracking. Lesion appearance is on “Scan 0.” Parameters at the lesion location (blue) are tracked over the 4 previous scans along with regional NAWM that does not evolve into a lesion (red). Even on the scan immediately preceding lesion appearance (“Scan -1”) there were no significant changes in any parameter that would allow lesion development to be anticipated beforehand.

III. KEY RESEARCH ACCOMPLISHMENTS:

- Developed novel method for simultaneous calibration of excitation flip angle and MT saturation power, thus improving the accuracy and longitudinal stability of MT imaging [1-2].
- Developed novel quantitative MT imaging method, “modified cross-relaxation imaging” (mCRI) [5], which decreases the number of acquired images and thus scan time relative to existing methods while yielding more accurate (by ~16%) values of macromolecular proton fraction, an imaging biomarker for myelin.
- Developed semi-automated image processing pipeline for longitudinal studies of multiparametric images, with key stages including co-registration across different modalities and time-points as well as tissue segmentation. This pipeline will be highly useful for any future studies involving longitudinal tracking of multiparametric imaging data.
- Achieved monthly tracking of multiple MRI metrics in treatment-naïve MS patients with active disease, allowing quantitative analysis of the natural history of lesion development.

IV. REPORTABLE OUTCOMES:

IV.A. Manuscripts:

- Hurley SA, Yarnykh VL, Johnson KM, Field AS, Alexander AL, Samsonov AA. Simultaneous variable flip angle-actual flip angle imaging method for improved accuracy and precision of three-dimensional T1 and B1 measurements. *Magn Reson Med* 2012;68(1):54-64.

- Mossahebi P, Yarnykh VL, Samsonov A. Analysis and correction of biases in cross-relaxation MRI due to biexponential longitudinal relaxation. *Magn Reson Med* 2014;71(2):830-838.

IV.B. Abstracts:

- Hurley SA, Mossahebi P, Johnson KM, Samsonov AA. Simultaneous Mapping of B1 and Flip Angle by Combined Bloch-Siegert, Actual Flip-Angle Imaging (BS-AFI). In: Proceedings of the International Society for Magnetic Resonance in Medicine (ISMRM) 20th Scientific Meeting, Melbourne, Australia, May 2012.
- Mossahebi P, Yarknykh VL, Samsonov AA. Improved Accuracy of Cross-Relaxation Imaging Using On-Resonance MT Effect Correction. In: Proceedings of the International Society for Magnetic Resonance in Medicine (ISMRM) 20th Scientific Meeting, Melbourne, Australia, May 2012.
- Mossahebi P, Samsonov AA. Optimization Strategies for Accurate Quantitative MT Imaging. In: Proceedings of the International Society for Magnetic Resonance in Medicine (ISMRM) 20th Scientific Meeting, Melbourne, Australia, May 2012.
- Samsonov AA, Mossahebi P, Anderson A, Velikina JV, Johnson KM, Johnson SC, Fleming JO, Field AS. High Resolution, Motion Corrected Mapping of Macromolecular Proton Fraction (MPF) In Clinically Acceptable Time Using 3D Undersampled Radials. In: Proc of ISMRM 2014; Milan, Italy. p 3337.
- Mossahebi P, Samsonov A. Rapid and Accurate Variable Flip Angle T1 Mapping with Correction of MT Effects. In: Proceedings of the International Society for Magnetic Resonance in Medicine (ISMRM) 20th Scientific Meeting, Melbourne, Australia, May 2012.

IV.C. Patents:

- “Efficient and Deterministic Approach to Generating Optimal Ordering of Diffusion MRI Measurements.” Patent applied for and awarded to Samuel A. Hurley, the graduate student who worked on the project and was supported by the award during his development of the invention. This is a novel ordering scheme for diffusion encoding gradients used to acquire diffusion-weighted MR images. The invention achieves increased efficiency of image acquisition several orders of magnitude greater than previously existing schemes.

IV.D. Degrees and Employment Opportunities

The graduate student who worked on the project, Samuel A. Hurley, received his Ph.D. in Medical Physics while supported by the award. He also successfully applied for a post-doctoral research scientist position at the University of Oxford Centre for Functional Magnetic Resonance Imaging of the Brain (FMRIB).

V. CONCLUSION:

The specific aim of the project was to acquire a longitudinal set of quantitative MRI metrics in MS patients and perform a multivariate spatiotemporal analysis of pre-lesional, normal-appearing white matter, seeking spatially clustered interval changes that presage the appearance of a typical MS plaque. Some previous studies have found such changes while others have not, and to date there is no known method for reliably predicting the location of a plaque before it is

visibly manifest. We did not find any pre-lesional changes that would make such prediction possible. Assuming such changes are indeed occurring, there are several possible reasons for failing to detect them which might be addressed in future work: (1) changes occurring on a spatial scale below current limits of MRI resolution; (2) changes occurring on a time scale shorter than the monthly intervals used for this study; or (3) changes occurring of a magnitude not exceeding technical inter-scan variance in MRI measurements, all of which are inherently “noisy” to some degree even with state-of-the-art acquisition and processing methods.

Although we were unable to achieve a prediction of MS lesions before they are visibly manifest (which would have been a major, paradigm-shifting advance in the management of MS patients), we did achieve several significant improvements in quantitative MRI methods important to the study of MS that will benefit future work in the field.

VI. REFERENCES:

1. Hurley SA, Yarnykh VL, Johnson KM, Field AS, Alexander AL, Samsonov AA. Simultaneous variable flip angle-actual flip angle imaging method for improved accuracy and precision of three-dimensional T1 and B1 measurements. *Magn Reson Med* 2012;68(1):54-64.
2. Hurley SA, Mossahebi P, Johnson KM, Samsonov AA. Simultaneous mapping of B1 and flip angle by combined Bloch-Siegert, actual flip-angle imaging (BS-AFI). In: Proceedings of the International Society for Magnetic Resonance in Medicine (ISMRM) 20th Scientific Meeting, Melbourne, Australia, May 2012.
3. Mossahebi P, Yarknykh VL, Samsonov AA. Improved accuracy of cross-relaxation imaging using on-resonance MT effect correction. In: Proceedings of the International Society for Magnetic Resonance in Medicine (ISMRM) 20th Scientific Meeting, Melbourne, Australia, May 2012.
4. Mossahebi P, Samsonov AA. Optimization strategies for accurate quantitative MT imaging. In: Proceedings of the International Society for Magnetic Resonance in Medicine (ISMRM) 20th Scientific Meeting, Melbourne, Australia, May 2012.
5. Mossahebi P, Yarnykh VL, Samsonov A. Analysis and correction of biases in cross-relaxation MRI due to biexponential longitudinal relaxation. *Magn Reson Med* 2014;71(2):830-838.
6. Samsonov AA, Mossahebi P, Anderson A, Velikina JV, Johnson KM, Johnson SC, Fleming JO, Field AS. High resolution, motion corrected mapping of macromolecular proton fraction (MPF) in clinically acceptable time using 3D undersampled radials. In: Proc of ISMRM 2014; Milan, Italy. p 3337.
7. Mossahebi P, Samsonov A. Rapid and accurate variable flip angle T1 mapping with correction of on-resonance MT effects. In: Proceedings of the International Society for Magnetic Resonance in Medicine (ISMRM) 20th Scientific Meeting, Melbourne, Australia, May 2012.

V. APPENDICES:

1. **Manuscript:** Simultaneous variable flip angle-actual flip angle imaging method for improved accuracy and precision of three-dimensional T1 and B1 measurements.

2. **Manuscript:** Analysis and correction of biases in cross-relaxation MRI due to biexponential longitudinal relaxation.
3. **Abstract:** Simultaneous mapping of B1 and flip angle by combined Bloch-Siegert, actual flip-angle imaging (BS-AFI).
4. **Abstract:** Improved accuracy of cross-relaxation imaging using on-resonance MT effect correction.
5. **Abstract:** Optimization strategies for accurate quantitative MT imaging.
6. **Abstract:** High resolution, motion corrected mapping of macromolecular proton fraction (MPF) in clinically acceptable time using 3D undersampled radials.
7. **Abstract:** Rapid and accurate variable flip angle T1 mapping with correction of on-resonance MT effects.

Simultaneous Variable Flip Angle–Actual Flip Angle Imaging Method for Improved Accuracy and Precision of Three-Dimensional T_1 and B_1 Measurements

Samuel A. Hurley,¹ Vasily L. Yarnykh,² Kevin M. Johnson,¹ Aaron S. Field,³ Andrew L. Alexander,^{1,4} and Alexey A. Samsonov^{3*}

A new time-efficient and accurate technique for simultaneous mapping of T_1 and B_1 is proposed based on a combination of the actual flip angle (FA) imaging and variable FA methods. Variable FA–actual FA imaging utilizes a single actual FA imaging and one or more spoiled gradient-echo acquisitions with a simultaneous nonlinear fitting procedure to yield accurate T_1/B_1 maps. The advantage of variable FA–actual FA imaging is high accuracy at either short T_1 times or long repetition times in the actual FA imaging sequence. Simulations show this method is accurate to 0.03% in FA and 0.07% in T_1 for ratios of repetition time to T_1 time over the range of 0.01–0.45. We show for the case of brain imaging that it is sufficient to use only one small FA spoiled gradient-echo acquisition, which results in reduced spoiling requirements and a significant scan time reduction compared to the original variable FA method. In vivo validation yielded high-quality 3D T_1 maps and T_1 measurements within 10% of previously published values and within a clinically acceptable scan time. The variable FA–actual FA imaging method will increase the accuracy and clinical feasibility of many quantitative MRI methods requiring T_1/B_1 mapping such as dynamic contrast enhanced perfusion and quantitative magnetization transfer imaging. Magn Reson Med 68:54–64, 2012. © 2011 Wiley Periodicals, Inc.

Key words: T_1 relaxometry; B_1 mapping; actual flip angle imaging (AFI); spoiled gradient echo

Accurate measurements of longitudinal relaxation time (T_1) are essential to many quantitative MRI techniques and clinical applications. Traditional inversion recovery T_1 mapping methods often result in prohibitively long acquisitions due to a long repetition time (TR) (1). The Look–Locker method (2) may be used to accelerate the inversion recovery experiment by frequent sampling of

the entire recovery curve. This two-dimensional (2D) approach can be modified to allow multislice volumetric coverage (3,4). A three-dimensional (3D) Look–Locker method (5) has also been proposed to improve the signal-to-noise ratio (SNR) and slice direction resolution of 2D techniques at the cost of blurring in phase encode directions due to segmented k -space acquisition.

The variable flip angle (VFA) method (6,7), also known as driven-equilibrium single-pulse observation of T_1 (DESPOT1) (7), uses several short TR spoiled gradient-echo (SPGR) acquisitions with varying flip angle (FA) to measure T_1 . It has gained significant popularity over the past decades due to its superior time efficiency, allowing rapid and accurate 3D T_1 mapping with high resolution and large spatial coverage (8–10). Although the acceleration of any T_1 mapping method is possible by the use of fast readout sequences (e.g., echo-planar or spiral) (11,12), applications of such techniques are limited to a large extent due to image artifacts inherent to long gradient-echo signal readouts. In contrast, VFA is the only fast T_1 mapping method to date that affords clinically reasonable scan times and 3D spatial coverage without a multiecho readout and, therefore, provides an optimal solution for high-resolution anatomic applications. In spite of these benefits, the VFA method suffers from a strong dependence on an accurate knowledge of excitation FA, which leads to significant errors in the presence of a nonuniform radiofrequency excitation field (B_1), slab excitation pulse profiles, or FA miscalibration (9,10,13). This is particularly problematic at high field strengths, where additional wave effects in tissue may cause B_1 variations up to 30% at 3 T and in situ FA calibration and correction is necessary on a per-subject basis (14).

It is therefore commonly accepted that VFA T_1 mapping at 3 T or higher field strengths needs to be combined with an appropriate B_1 correction method (9,10), and many methods to measure FA have been developed and applied to the correction of VFA T_1 measurements. Similar to inversion recovery-based T_1 mapping techniques, the double angle method (15) uses a 2D multislice acquisition with a long TR to avoid T_1 weighting of the acquired maps. Scan time can be reduced by minimizing T_1 dependence with specialized radiofrequency presaturation pulses (16,17) to achieve a uniform saturation of magnetization over a large area prior to readout. However, the 2D implementation imposes restrictions on the use of double angle method as a correction technique for 3D VFA T_1 measurements due to slice profile effects.

¹Department of Medical Physics, University of Wisconsin, Madison, Wisconsin, USA.

²Department of Radiology, University of Washington, Seattle, Washington, USA.

³Department of Radiology, University of Wisconsin, Madison, Wisconsin, USA.

⁴Department of Psychiatry, University of Wisconsin, Madison, Wisconsin, USA.

Grant sponsor: NIH NINDS; Grant number: R01NS065034; Grant sponsor: NIBIB; Grant number: R21EB009908.

*Correspondence to: Alexey A. Samsonov, Ph.D., Wisconsin Institutes of Medical Research, 1111 Highland Ave, Rm. 1117, Madison, WI 53705. E-mail: samsonov@wisc.edu

Received 21 May 2011; revised 1 August 2011; accepted 4 August 2011.

DOI 10.1002/mrm.23199

Published online 2 December 2011 in Wiley Online Library (wileyonlinelibrary.com).

It is important to note that a 3D B_1 mapping technique with matched geometry is preferable in the context of VFA T_1 mapping to simplify registration between data volumes. One 3D approach encodes the FA in the phase of the MR signal (18). This reduces the T_1 dependence due to previous magnetization history and can image over a large dynamic range of FA, but is sensitive to main field inhomogeneity and requires a long TR relative to T_1 to avoid phase oscillations. Other fast techniques have recently been proposed based on a stimulated-echo echo-planar acquisition (19) and a modification of double angle method using a catalyzed preparative sequence (20). Methods that use a steady-state gradient echo readout are particularly well suited as these pulse sequences are closely related to the SPGR sequence used in VFA and can, therefore, be acquired with the same matrix size and readout scheme, greatly increasing the consistency between the FA and T_1 mapping steps. Such methods include a multipoint search of the signal null corresponding to the 180° FA (21,22), a B_1 -dependant shift in the spin resonance frequency (23), an inversion-recovery SPGR termed driven equilibrium single-pulse observation of T_1 with high-speed incorporation of radiofrequency (RF) field inhomogeneities (DESPOT1-HIFI) (24), and a dual TR SPGR acquisition termed actual flip angle imaging (AFI) (25).

The accurate combination of a B_1 mapping technique with 3D VFA T_1 mapping requires consideration of additional factors affecting FA values, including excitation slab/slice profile and RF pulse properties (26). Two recently proposed methods, DESPOT1-HIFI (24) and AFI (25), measure FA using the exact same excitation pulse envelope and slab geometry as the VFA experiment, allowing measurements with a very similar FA distribution present in both sequences. DESPOT1-HIFI requires an additional B_1 -insensitive adiabatic inversion preparation, which, with proper tuning of the inversion time to the expected T_1 range, enables fast and accurate FA mapping. To avoid T_1 weighting, the AFI method estimates FA maps using the ratio of two signals from two different TR s ($TR_{AFI1,2}$) using a linearized form of the signal equation (see next section), which holds under a main assumption that

$$TR_{AFI1,2} \ll T_1 \quad [1]$$

The calculated FA map can then be applied as a precalibration step to a traditional VFA T_1 measurement. AFI is well suited for the correction of VFA measurements because of the identical readout scheme to the SPGR pulse sequence, the use of an identical RF excitation pulse, and lack of a need for additional magnetization preparation with specialized RF pulses (20,23,24).

In spite of the many benefits of AFI, recent studies have shown that large spoiler gradients are required for effective suppression (spoiling) of transverse magnetization and thus accurate FA measurements (27). Such large gradients require a considerable increase in the TR compared to a standard short TR SPGR sequence and, therefore, an overall increase in scan time. Although proper spoiling is essential for accurate FA quantification, increasing the TR of the AFI sequence may lead to a violation of the main assumption (Eq. 1) (25), posing another significant problem with the accuracy and over-

all efficiency of the technique. Similarly, strong spoiler gradients are also necessary in VFA SPGR measurements for accurate T_1 mapping, especially at larger FAs (27,28). This further increases the overall time of the technique.

An independent mechanism for violation of the AFI assumption (Eq. 1) is T_1 shortening due to contrast agents, which may render postcontrast FA measurements highly inaccurate. Postcontrast T_1 measurements should therefore be corrected with a precontrast B_1 map. However, this is not feasible in some applications, such as manganese-enhanced MRI of axon pathways, which requires injection of a contrast agent ~ 24 h before the scan (29). A wide range of applications would greatly benefit from a rapid and accurate method to measure T_1 and FA in the presence of T_1 -shortening contrast agents (30,31).

AFI and VFA are highly complementary methods; AFI suffers inaccuracies due to an assumption about T_1 , whereas VFA suffers inaccuracies due to an assumption about FA. In this article, we propose an efficient method to tackle the quantification of T_1 and B_1 in the problematic AFI regime ($TR_{AFI1,2} \approx T_1$) arising from a long AFI TR due to spoiling requirements and/or short T_1 times. In our method, variable flip angle–actual flip angle imaging (VAFI), T_1 and B_1 are mapped simultaneously using an optimized combination of AFI and VFA SPGR acquisitions. By exploiting the close relationship of the SPGR and AFI signal equations, we demonstrate that the $TR_{AFI1,2} \ll T_1$ assumption is not necessary when T_1 and B_1 are mapped simultaneously, resulting in a high FA mapping accuracy over a broad range of T_1 (32), an improvement in the precision of T_1 and B_1 measurements, and increased time efficiency of such measurements. We also show that VAFI reduces the spoiling requirements of the SPGR portion of the method, allowing a shorter TR and overall decrease in acquisition time.

THEORY

Variable Flip Angle T_1 Mapping

T_1 measurements based on VFA SPGR acquisitions have been previously described in (6–8,33). Given ideal spoiling of transverse magnetization, the SPGR signal can be described as follows:

$$S_{SPGR} = M_0 \sin(\alpha) \frac{1 - E_1}{1 - E_1 \cos(\alpha)}, \quad [2]$$

$$E_1 = \exp\left(\frac{-TR}{T_1}\right)$$

where TR and excitation FA α are control parameters prescribed from the operator console, and the equilibrium magnetization M_0 and T_1 are free parameters to be determined. Here, we assume that M_0 absorbs additional factors due to T_2^* relaxation, receiver gains, and coil sensitivity profile. In VFA T_1 mapping, two or more acquisitions with varying α and fixed TR are acquired and fitted to yield M_0 and T_1 . The problem of data fitting can be conveniently casted into a linear form and fitted with least squares regression (8) or the curve can be fitted directly using nonlinear methods, with the latter approach in general providing better noise performance (34). In practice, two “ideal” FAs are enough to provide

optimized VFA T_1 mapping for a given T_1 value (33), the lower FA yielding an image with proton-density like contrast and higher FA with T_1 -like contrast.

Actual Flip Angle Imaging

The AFI sequence is a spoiled gradient-recalled echo acquisition with two identical excitation RF pulses with FA α separated by two interleaved repetitions times $TR_{AFI1,2}$ (25). Given complete spoiling of transverse magnetization at the end of each TR (25), the steady-state signal from the AFI sequence is described by the following equations:

$$S_{AFI1,2} = M_0 \sin(\alpha_{AFI}) \times \frac{1 - E_1^{(AFI2,1)} + (1 - E_1^{(AFI1,2)}) E_1^{(AFI1,2)} \cos(\alpha_{AFI})}{1 - E_1^{(AFI1,2)} E_1^{(AFI2,1)} \cos^2(\alpha_{AFI})}. \quad [3]$$

$$E_1^{(AFI1,2)} = \exp\left(\frac{-TR_{AFI1,2}}{T_1}\right)$$

It was shown in (25) that under the condition of Eq. 1 there exists an efficient first-order exponential approximation without an explicit dependence on M_0 or T_1 . The signal then can be solved for the FA as follows:

$$\alpha_{AFI} = \arccos\left(\frac{rn - 1}{n - r}\right). \quad [4]$$

$$n = TR_{AFI2}/TR_{AFI1}, \quad r = S_{AFI2}/S_{AFI1}$$

Variable Flip Angle–Actual Flip Angle Imaging

To avoid the main AFI assumption (Eq. 1), we propose a novel approach, VAFI, which takes as an input one AFI dataset and one or more VFA SPGR datasets. In VAFI, the dependence of the AFI FA on T_1 is not ignored, but instead coupled in a single nonlinear optimization procedure for an unbiased simultaneous estimation of both parameters. We assume that M_0 is consistent between SPGR and AFI acquisitions (Eqs. 2 and 3, respectively), which requires that the RF excitation pulse, slab selection gradient, and echo times be identical for both the SPGR and AFI pulse sequences, and that the signal from both pulse sequences is perfectly spoiled (25,27). Additionally, we assume that error in α scales linearly with transmit field across the range of FAs used in the VFA and AFI measurements. This assumption has been made in many previous FA mapping techniques (15–17), and recent Bloch equation simulation results have shown less than 4% deviation from linearity over a range of 2° – 70° (35). For a set of SPGR FAs α_i and an AFI FA α_{AFI} with corresponding observed signals $S_{SPGR,i}$ and $S_{AFI1,2}$, the unknown parameters can be determined on a per-pixel basis by simultaneously fitting both the SPGR and AFI signal models using nonlinear least squares:

$$[M_0 \ T_1 \ \kappa] = \arg \min_{M_0 \ T_1 \ \kappa} \left(\sum_{i=1}^2 (S_{AFI,i} - S_{AFI,i}(\alpha_{AFI} \cdot \kappa))^2 + \sum_{i=1}^{N_{SPGR}} (S_{SPGR,i} - S_{SPGR}(\alpha_i \cdot \kappa))^2 \right), \quad [5]$$

where $\arg \min(f(x))$ is the set of values x for which $f(x)$ attains its smallest value.

This procedure simultaneously yields a solution for three unknown parameters: M_0 , T_1 , and κ , where κ is a scaling factor between actual and prescribed FA. Theoretically, this sets the lower limit on the total number of required measurements to three. As a single AFI sequence yields two independent measurements, we anticipate the minimum number of SPGR measurements to be one. As AFI requires a large FA (50° – 60°) to optimize the estimation of FA maps and yields images with T_1 -like contrast, we anticipate that the SPGR measurement with the larger FA may be removed compared to the standard VFA experiment design (8,33).

As the transmit field varies slowly with spatial position, an additional term may be introduced to Eq. 5 to penalize the roughness of $\kappa(r)$ and improve the noise properties of reconstructed parametric maps in a way similar to regularized fat/water imaging (36), which may be computationally challenging for 3D reconstructions. To reduce computational time, we developed a simplified three-step version of the regularization procedure:

Step 1: Solve Eq. 5 for spatial maps $[M_0 \ T_1 \ \kappa]$

Step 2: Apply spatial smoothing to $\kappa(r)$ to yield $\kappa_s(r)$.

Step 3: Solve $[M_0 \ T_1] = \arg \min_{M_0 \ T_1} \left(\sum_{i=1}^2 (S_{AFI,i} - S_{AFI,i}(\alpha_{AFI} \cdot \kappa_s))^2 + \sum_{i=1}^{N_{SPGR}} (S_{SPGR,i} - S_{SPGR}(\alpha_i \cdot \kappa_s))^2 \right)$.

MATERIALS AND METHODS

Implementation

The proposed VAFI fitting method was implemented in MATLAB (The Mathworks; Natick, MA) using a built-in optimization algorithm. As an initial guess, we used the maximum signal intensity for M_0 , $T_1 = 1$ s, and $\kappa = 1$. VAFI converged properly for all simulations and experiments without a need to modify this initial guess. Typical processing time was ~ 42 ms per voxel (64-bit Intel Linux workstation, 4 cores, 32 GB RAM). In step 2 of the regularized VAFI and standard AFI approaches, a local polynomial fit was applied to generate smoothed and extrapolated FA maps (37) with a smoothing effect equivalent to a gaussian kernel with a standard deviation of four voxels. For comparison, T_1 and FA maps were generated using standard AFI-corrected VFA with linearized T_1 estimation and iterative reweighting (34).

An AFI pulse sequence was implemented on a clinical GE 3.0T Discovery MR750 (GE Healthcare; Waukesha, WI) based on a product 3D SPGR sequence with the addition of a second TR as described in (25). Experiments were performed using a 32-element phased-array receive coil (*in vivo* experiments) and an eight-element torso coil (phantom experiments). Spoiler gradients were designed such that their areas $A_{G1,2}$ were related as $A_{G2} = nA_{G1}$ (Eq. 4). RF spoiling was used with a quadratic phase increment of 34° (27). For all experiments, $n = TR_{AFI2}/TR_{AFI1} = 5$, as was suggested in previous work (25). The specific strengths of the spoiler gradients were

chosen based on the completeness of spoiling desired, herein referred to as “spoiling regime.”

Simulations

Monte Carlo noise simulations were implemented to compare the accuracy (bias in the estimated values) and precision (noise in the estimated values) of standard two FA VFA with AFI correction (henceforth referred to as VFA) and VAFI. AFI and SPGR signals were generated using Eqs. 2 and 3, with simulation parameters chosen to match the *in vivo* experiments described in the next section (SPGR: $TR = 10$ ms, $\alpha = [3\ 18]^\circ$; AFI: $TR_{AFI1} = 30$ ms, $\alpha_{AFI} = 55^\circ$). Signals were generated over a range of $TR/T_1 = 0.01$ – 0.45 , and for each T_1 time 250,000 noise realizations were created by adding zero-mean gaussian noise (standard deviation of $1e^{-4}$) to the signals. VAFI was implemented using the smallest SPGR FA signal and, to allow an equivalent comparison with VFA, using both SPGR FAs. T_1 and FA were then estimated to assess the accuracy and precision of all three approaches, the latter being assessed in terms of the T_1 -to-noise and α -to-noise ratios (T_1 NR and α NR).

A second simulation was performed to investigate the effect of FA selection on the VAFI experiment. For two-angle VFA, a pair of “ideal angles” has been previously identified as a way to optimize experiment design for a specific T_1 ; however, these angles were derived based on the linearized version of the SPGR equation (33), which is no longer valid in the VAFI technique. To assess the noise performance of our new method, a set of 45,000 noise realizations (standard deviation of $1e^{-4}$) were generated over a range of $TR/T_1 = 0.02$ – 0.15 . In the first set of simulations, α_{AFI} was held constant at 55° while the SPGR FA was varied over a range of 1° – 20° . In the second set, SPGR FA was held constant at 5° while α_{AFI} was varied over a range of 40° – 70° . All other parameters match the previous simulation.

A third simulation was performed to evaluate the effect of gradient and RF spoiling on the accuracy of VAFI quantification. AFI and SPGR signals were generated using a combined isochromat summation and diffusion propagator model (27), which takes into account transverse signal dephasing due to both gradient and diffusion effects. Signals were generated for prototypical tissues at 3 T over a range of RF phase increments $\phi_0 = 0^\circ$ – 180° (white matter (WM): $T_1/T_2 = 1000/70$ ms, diffusion coefficient $D = 0.70 \times 10^{-3}$ mm²/s; gray matter (GM): $T_1/T_2 = 1500/100$ ms, $D = 0.80 \times 10^{-3}$ mm²/s; cerebrospinal fluid (CSF): $T_1/T_2 = 4000/1900$ ms, $D = 3.00 \times 10^{-3}$ mm²/s). SPGR signals were simulated using $\alpha = [3\ 18]^\circ$ for three spoiling regimes: weak ($TR = 10$ ms, $A_G = 38$ mT*ms/m), strong ($TR = 10$ ms, $A_G = 110$ mT*ms/m), and nearly complete spoiling ($TR = 15$ ms, $A_G = 280$ mT*ms/m). AFI signals were generated using $\alpha_{AFI} = 55^\circ$ for weak ($TR_{AFI1,2} = 10/50$ ms, $A_{G1} = 38$ mT*ms/m), intermediate ($TR_{AFI1,2} = 10/50$ ms, $A_{G1} = 110$ mT*ms/m), strong ($TR_{AFI1,2} = 15/75$ ms, $A_{G1} = 280$ mT*ms/m), and nearly complete spoiling ($TR_{AFI1,2} = 30/150$ ms, $A_{G1} = 450$ mT*ms/m). The data were then fitted using the VFA and VAFI (single SPGR measurement, $\alpha = 3^\circ$) methods in two ways, one assuming ideal AFI spoiling with noni-

deal SPGR data, and one assuming ideal SPGR spoiling using nonideal AFI data. The accuracy of T_1 estimates was then assessed.

Phantom Experiments

To test the effects of the suboptimal AFI regime ($TR \approx T_1$) on both VFA and VAFI, a set of 10 phantoms were created from deionized water doped with Gd-BOPTA to concentrations of $C = [0.00\ 0.10\ 0.25\ 0.50\ 1.00\ 2.00\ 2.50\ 3.00\ 3.50\ 4.00]$ mM. The phantoms were placed in a heated water bath lightly doped with Gd-BOPTA and held at $36.8^\circ\text{C} \pm 0.5^\circ\text{C}$ for the duration of the experiment. SPGR scans were acquired with $TR = 25$ ms and $\alpha = [4\ 10\ 20\ 30\ 40\ 50]^\circ$ and an AFI scan with $TR_{AFI1} = 30$ ms, $\alpha_{AFI} = 55^\circ$ in the nearly complete spoiling regime. Voxel size was $2.2 \times 2.2 \times 2$ mm³. All SPGR FAs were used in VFA and VAFI to ensure a precise measurement over the wide range of expected T_1 times. The mean and standard deviation of R_1 ($=1/T_1$) were calculated in a single slice region of interest encompassing each individual phantom and used to fit the equation:

$$R_1(C) = R_{1,0} + r_1 \cdot C, \quad [6]$$

where r_1 is the relaxivity, and $R_{1,0}$ is longitudinal relaxation rate for free water. The linear fit was weighted according to the measured variance in the R_1 values.

It was shown before that simultaneously increasing TR and acceleration factor R while maintaining a constant acquisition time constant leads to an improvement of the overall SNR efficiency of several steady-state gradient-echo techniques (38). In the context of AFI, in addition to signal boost from longer TR , this increase also offers an opportunity to increase the length of the spoiler gradient and improve the accuracy of FA quantification (27). To confirm this effect for the AFI sequence, a uniform bottle phantom doped with Gd-DTPA to a T_1 of 1.4 s was scanned using an eight-channel receive-only phased array knee coil. Two AFI scans were acquired ($\alpha_{AFI} = 55^\circ$, nearly complete spoiling with $TR = 30$ ms, and weak spoiling with $TR = 10$ ms, 1.5 mm³ voxel). The $TR = 30$ ms data was subsequently undersampled by a factor of 3 in the phase encode direction and reconstructed with sensitivity encoding (SENSE), such that the experiment time matched AFI with $TR = 10$ ms. FA maps using weakly spoiled AFI ($TR = 10$ ms) were also generated for comparison. Noise in the resulting FA maps was estimated by taking the standard deviation in a small region of interest over the center of the bottle to avoid regions of artifact in the poorly spoiled AFI image.

In Vivo Imaging

To demonstrate the application of VAFI to *in vivo* brain imaging, one healthy human volunteer was scanned. Informed written consent was obtained in accordance with the local institutional policy. SPGR scans were acquired with $TR = 10$ ms and $\alpha_{SPGR} = [3\ 18]^\circ$, which is optimal for $T_1 = 1.2$ s as described in (33). To demonstrate the benefits of increased TR on spoiling, two AFI

scans were acquired with $\alpha_{AFI} = 55^\circ$ in the weak regime ($TR_{AFI1,2} = 10/50$ ms, $A_{G1} = 38$ mT*ms/m) and in the complete regime ($TR_{AFI1,2} = 30/150$ ms, $A_{G1} = 450$ mT*ms/m). The last AFI scan was repeated with SENSE (37) acceleration factor $R = 3$ to demonstrate the feasibility of an overall scan time reduction. All scans were acquired with a $128 \times 96 \times 44$ matrix and an isotropic resolution of $2 \times 2 \times 2$ mm³ placed near the center of the brain. The scan time was 1:30 min for SPGR, 4:13 min for AFI with $TR_{AFI1,2} = 10/50$ ms, and 12:40 min for AFI with $TR_{AFI1,2} = 30/150$ ms and $R = 1$. For AFI with $R = 3$, the scan time was 4:13 min.

RESULTS

Simulations

Figure 1 shows the results of simulations comparing the accuracy and precision of the methods. Over the range investigated, the standard AFI method shows a systematic underestimation of FA with decreasing T_1 (>5% for $TR/T_1 > 0.275$). VAFI FA errors were less than 0.03%. T_1 estimates for VFA were systematically overestimated at small TR/T_1 , due to propagation of AFI errors into VFA T_1 mapping (>5% for $TR/T_1 > 0.160$). VAFI was able to restore the accuracy of T_1 estimates (errors less than 0.07%). T_1 NR of VAFI exceeded that of AFI for a $TR/T_1 < 0.085$, and α NR was comparable for $TR/T_1 < 0.150$. For shorter T_1 , the AFI method actually shows better noise properties of FA estimates than VAFI; however, this may be artifactual as in this region the FA and T_1 estimates are also highly inaccurate and generally not useful. The peak T_1 NR with these particular settings was observed for a TR/T_1 of 0.06; however, it will be noted in the next paragraph that T_1 NR can be optimized for a

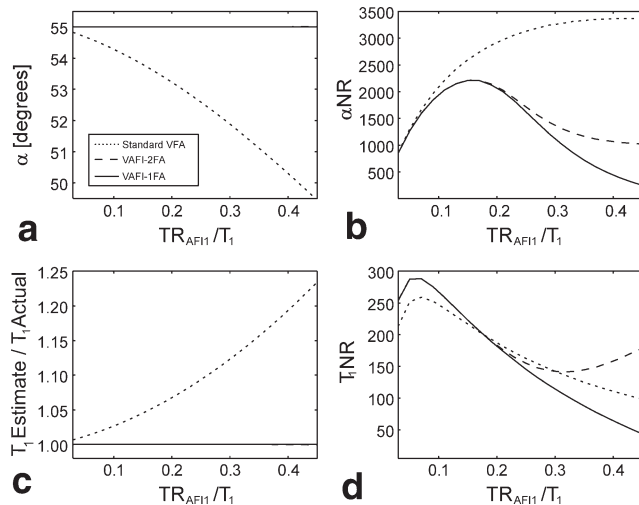


FIG. 1. Monte Carlo simulations of standard VFA (dotted line) and VAFI (dash line for two flip angle fit and solid line for one flip angle fit) over a range of TR_{AFI1}/T_1 for flip angle accuracy (a), flip angle-to-noise ratio (b), T_1 accuracy (c), and T_1 -to-noise-ratio (d). Results show a significant underestimation of FA for short T_1 times, which will propagate into standard VFA measurements, causing an overestimation of T_1 . VAFI remains accurate over the entire range investigated for both one and two SPGR flip angle options.

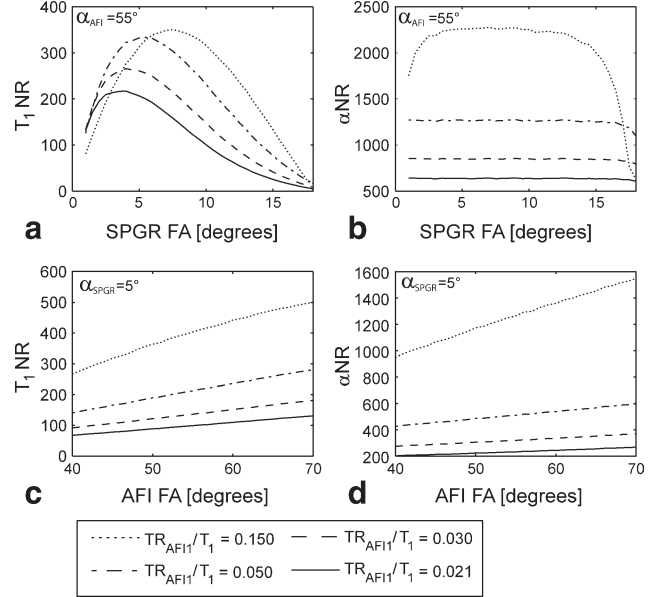


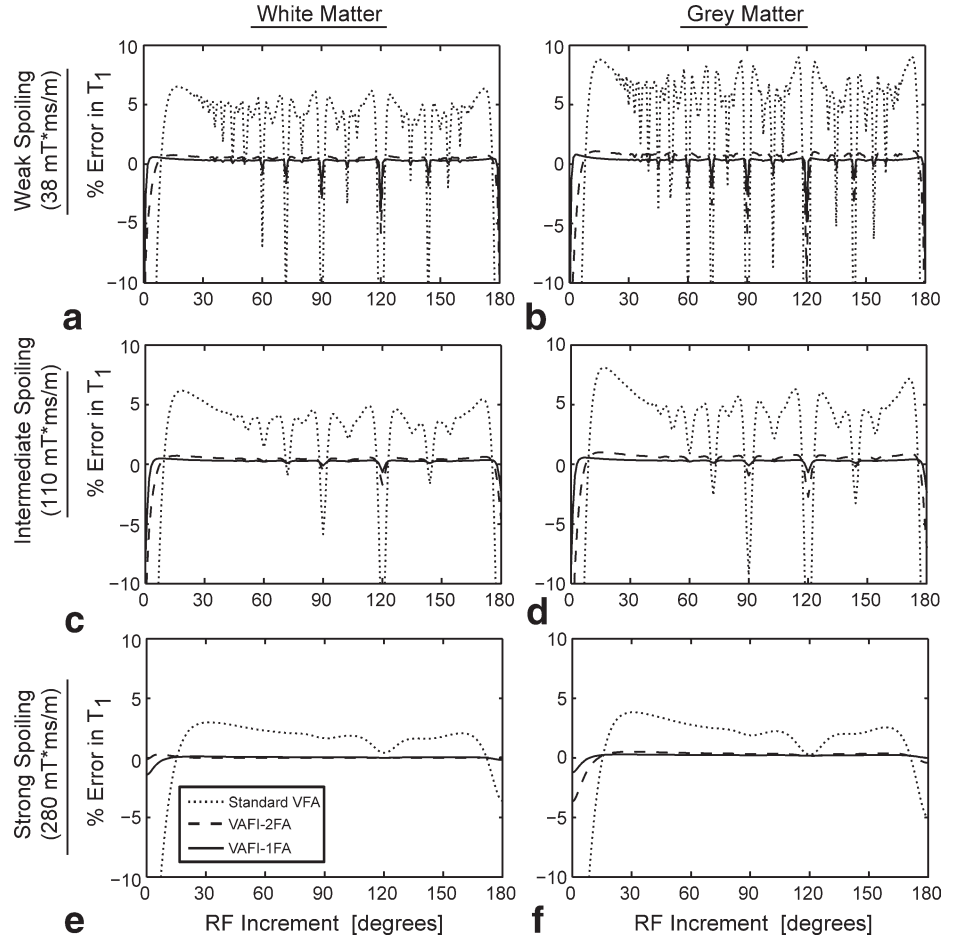
FIG. 2. Monte Carlo simulations demonstrating the impact of flip angle selection in the VAFI technique on the T_1 -to-noise-ratio (a, c) and flip angle-to-noise-ratio (b, d) for a $TR_{AFI1}/T_1 = 0.150$ (dotted line), 0.050 (dot-dash line), 0.030 (dash line), and 0.021 (solid line). As is the case for VFA, there exists an SPGR flip angle which optimizes precision (a).

specific T_1 of interest by the choice of an appropriate SPGR FA. Remarkably, VAFI with two SPGR measurements shows more uniform noise performance in the range of TR/T_1 than VAFI with single SPGR measurements, which is consistent with improved uniformity of noise performance of VFA T_1 mapping with extended set of SPGR measurements (more than two) (39).

Figure 2 shows the results of VAFI T_1 NR and α NR as a function of TR/T_1 and SPGR FA. The choice of FA has an impact on the T_1 NR, and just as the case for standard VFA, there exists an optimum angle that maximizes precision for a given T_1 time. The optimum angles for $T_1 = 200, 600, 1000$, and 1400 ms were $7.5^\circ, 5.5^\circ, 4^\circ$, and 3.5° , respectively ($TR = 10$ ms). As long as the SPGR FA is within a reasonable range about the optimum value, there is no significant impact on the precision of the FA estimate. The choice of AFI FA has considerable impact on the precision of both VAFI T_1 and FA measurements, although in this case there is no single optimum value for a specific T_1 time; the precision of both T_1 and FA increases linearly as AFI FA increases.

Figure 3 shows the results of simulations assuming ideal AFI spoiling and nonideal SPGR spoiling for WM and GM tissues. For standard VFA, increasing the gradient spoiling minimizes the dependence of T_1 accuracy on the RF phase increment. However, the choice of a proper phase increment (i.e., the choice of ϕ_0 which crosses or approaches the zero axis) and its accuracy and stability remains essential for accurate quantification. In contrast, the use of VAFI greatly reduces spoiling-related errors over a wide range of phase increments, even in the weak SPGR spoiling regime. Specifically, in the weak SPGR spoiling regime, if one chooses a phase

FIG. 3. Simulation results showing the dependence of T_1 accuracy on SPGR phase increment for weak (a, b), intermediate (c, d), and strong (e, f) spoiling regimes in prototypical WM ($T_1/T_2 = 1000/70$ ms, $D = 0.70 \times 10^{-3}$ mm²/s) (a, c, e) and gray matter ($T_1/T_2 = 1500/100$ ms, $D = 0.80 \times 10^{-3}$ mm²/s) (b, d, f) tissues using standard VFA (dotted line) and VAFI (dash line for two flip angle fit, solid line for one flip angle fit). Simulations assume an ideally spoiled AFI acquisition. Results for CSF show similar profiles (not shown). Results show that spoiling errors and dependence on proper phase increment are greatly reduced for the VAFI technique with the best performance achieved for the single flip angle VAFI fit.



increment that does not fall near one of the sharp peaks (ex: $\phi_0 = 10^\circ$ – 35°), VAFI with two SPGR FAs achieves an error in T_1 estimates of $<0.80\%$ (WM), $<1.10\%$ (GM), and $<1.75\%$ (CSF, not shown in plot) and an error in FA $<0.26\%$ (all tissues). Remarkably, these errors and the dependency on the phase increment are further reduced in VAFI with single SPGR FA (T_1 errors: $<0.54\%$ in WM, $<0.60\%$ in GM, and $<0.32\%$ in CSF). The intermediate and strong spoiling regimes produce similar results, with fewer sharp peaks to avoid.

Figure 4 shows the results of simulations assuming nonideal AFI spoiling and ideal SPGR spoiling for WM and GM. The behavior of spoiling-related errors is similar for the VFA and VAFI. Unlike the case of SPGR spoiling, the choice of a proper AFI phase increment is essential for accurate FA and T_1 quantification for all techniques. The proper phase increment (i.e., the choice of ϕ_0 which crosses zero axis) depends on the spoiling regime, tissue type, and estimation technique used. For weak spoiled AFI, the optimal values of ϕ_0 are 29° (WM), 20° (GM), and 50° (CSF), whereas in the nearly complete spoiling regime, these values are 39° (WM), 41° (GM), and any ϕ_0 for CSF (not shown in plot). For the VAFI technique in the weak regime, these values are 30° (WM), 25° (GM), and 55° (CSF), whereas in the nearly complete regime these values are 43° (WM), 44° (GM), and any ϕ_0 for CSF. However, small deviations in ϕ_0 about the optimal value produce minimal errors in FA

and T_1 accuracy for all tissues when the nearly complete AFI regime is used.

Phantom Experiments

Figure 5 compares FA maps in Gd phantoms estimated using standard AFI and VAFI. A significant discontinuity between the short T_1 vials (phantoms 6–10) and the background media (longer T_1) can be observed in the AFI FA map (Fig. 5a). These errors, which are due to a violation of the AFI assumption (Eq. 1), are minimized in the VAFI FA map (Fig. 5b), which agrees well with the expected slowly varying value of FA in the imaging plane. The growing differences between local FA values of AFI and VAFI with Gd concentration may be appreciated in Table 1. A similar trend may be observed in the calculated T_1 values, with T_1 errors reaching 19% for the highest Gd concentration. Corresponding R_1 measurements versus Gd concentration show expected linear relaxivity curves (Eq. 6) for VAFI (Fig. 6). The VAFI-derived relaxivity for the Gd-BOPTA solution was $3.9361 \text{ s}^{-1} \text{ mM}^{-1}$ ($R^2 = 0.9996$), which compares well to the reference value of $4.0 \text{ s}^{-1} \text{ mM}^{-1}$ at 37°C (personal communication with Dr. Sophie Laurent, NMR and Molecular Imaging Laboratory, University of Mons, Belgium). This relaxivity measurement was significantly underestimated by standard AFI VFA ($r_1 = 3.5192 \text{ s}^{-1} \text{ mM}^{-1}$, $R^2 = 0.9935$).

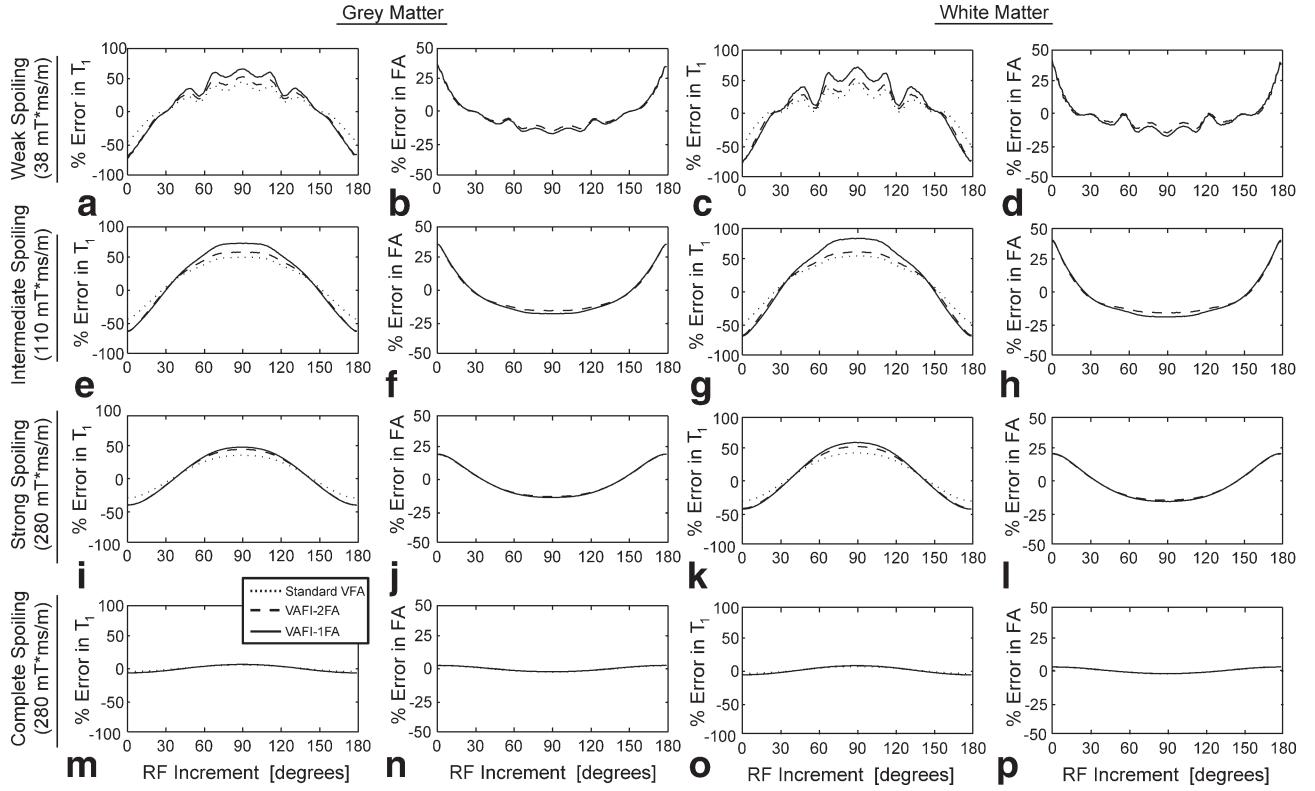


FIG. 4. Simulation results showing the dependence of T_1 and flip angle accuracy on AFI RF phase increment for weak (a–d), intermediate (e–h), strong (i–l), and nearly complete (m–p) gradient spoiling (see text for details) using standard (dotted line) and VAFI (dash line for two flip angle fit, solid line for one flip angle fit).

Figure 7 illustrates the effect of increasing the SENSE acceleration factor on the accuracy and precision of AFI maps for the strong spoiling regime and a comparison with an AFI map in the short TR (weak spoiling) regime. Simulated AFI steady-state signals grow with increasing TR faster than the SNR loss due to R -factor, giving rise to an overall increase in SNR efficiency for realistic reduction factors ($R < 8$) and constant scan time (Fig. 7a). Indeed, long TR (strong spoiling) AFI (Fig. 7b) demonstrates improved precision over a short TR (weak spoiling) AFI (Fig. 7c) obtained in an equivalent scan time ($R = 3$). The weak spoiling regime in the short TR AFI also leads to significant artifacts in the estimated FA map (Fig. 7c).

In Vivo Imaging

Figure 8 shows a representative axial T_1 map from the *in vivo* experiment using fully sampled well-spoiled (Fig. 8a,b) and poorly spoiled (Fig. 8d,e) AFI sequences. Table 2 shows the values taken from region of interests positioned in WM, GM, and CSF. For the weak AFI spoiling regime ($TR_1 = 10$ ms), incomplete spoiling leads to underestimated FA measurements and overestimated T_1 for all tissues, which is in accordance with theoretical predictions (see Fig. 4 and Ref. 27). In the complete spoiling regime, both VFA and VAFI compare similarly to previously published values in the selected WM/GM

region of interests (40), while VAFI reaches comparable or even better precision in less time (using one less SPGR measurement). Remarkably, in CSF, VAFI provided superior accuracy of T_1 estimates based on the previously published reference CSF T_1 values at 3 T (41). The errors observed for the standard VFA method may be due to the fact that the spoiling regime used in this experiment resulted in incomplete spoiling for the higher SPGR FA and nearly complete spoiling for the smaller SPGR FA. Because VAFI uses only the smaller SPGR FA, the spoiling errors in SPGR are less likely to affect T_1 estimates, as also follows from the theoretical

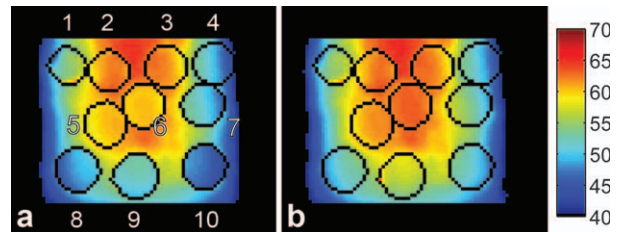


FIG. 5. A map of flip angle, in degrees, of the T_1 phantom generated using the standard AFI (a) and VAFI (b) techniques. The nominal FA was 55° (see Table 1 for vial labeling). A significant error not related to the slowly varying B_1 spatial distribution can be seen in the standard case (a), where a significant discontinuity in measured FA exists between the background media and very short T_1 vials (#5–10). This error is corrected using the VAFI technique (b).

Table 1

Vial Numbers, Gd-BOPTA Concentrations, T_1 , and FA Measurements from the T_1 Phantom (see Fig. 7)

Vial #	Gd Conc. (mM)	T_1 VFA (s) \pm Stdev	T_1 VAFI (s) \pm Stdev	FA AFI ($^\circ$) \pm Stdev	FA VAFI ($^\circ$) \pm Stdev
1	0.00	4.181 \pm 0.403	4.057 \pm 0.269	54.1 \pm 2.04	54.8 \pm 1.97
2	0.10	1.523 \pm 0.085	1.494 \pm 0.071	61.8 \pm 1.04	62.0 \pm 1.06
3	0.25	0.811 \pm 0.032	0.790 \pm 0.021	61.6 \pm 0.97	62.0 \pm 0.99
4	0.50	0.451 \pm 0.014	0.432 \pm 0.012	49.3 \pm 1.97	49.7 \pm 2.03
5	1.00	0.247 \pm 0.008	0.230 \pm 0.008	60.1 \pm 0.51	61.4 \pm 0.51
6	2.00	0.137 \pm 0.004	0.122 \pm 0.002	60.2 \pm 0.24	63.1 \pm 0.27
7	2.50	0.111 \pm 0.004	0.097 \pm 0.002	50.9 \pm 1.38	53.7 \pm 1.53
8	3.00	0.093 \pm 0.003	0.083 \pm 0.001	48.6 \pm 0.93	51.8 \pm 1.10
9	3.50	0.086 \pm 0.003	0.072 \pm 0.001	51.9 \pm 0.72	56.6 \pm 0.86
10	4.00	0.079 \pm 0.004	0.064 \pm 0.001	46.6 \pm 1.05	51.2 \pm 1.29

analysis (see Fig. 3). Finally, we demonstrate a SENSE-accelerated, well-spoiled T_1 map using VAFI, which shows high image quality (Fig. 8c) and T_1 values (Table 2) comparable to the nonaccelerated VAFI (Fig. 8b).

DISCUSSION

The VFA SPGR T_1 mapping continues to be an accurate and efficient method for mapping T_1 over a large 3D volume; however, a large limitation to this technique is the need for an accurate estimate of an actual FA, especially at higher field strengths (3 T and above). Among many methods for measuring FA, AFI (25) has emerged as a very attractive choice for correcting VFA measurements because of its high time efficiency and similar pulse sequence design. In spite of these benefits, AFI often presents its own limitations due to the need for a short TR to maintain the validity of the $TR_{AFI,2} \ll T_1$ assumption. The available tradeoffs may lead to inaccurate FA and T_1 mapping and elongated acquisition times in some practical applications. We presented a novel technique, VAFI, that provides a T_1 -independent FA map and simultaneously yields accurate T_1 values. Briefly described in (32), VAFI maintains high accuracy in regimes that are problematic for the standard AFI tech-

nique ($TR \approx T_1$), allowing its use in applications involving a long TR (for proper spoiling) or with T_1 -shortening contrast agents (such as dynamic contrast-enhanced imaging). It was previously noted that the VFA technique alone provides no unique solution for M_0 , T_1 , and FA (13). With the addition of dual- TR AFI data, a unique solution can be found even with only a single SPGR data point. An interesting approach to yield both FA and T_1 values was proposed in subsequent work, which generalizes AFI into a pulse sequence of N arbitrary TR periods (42). The practical advantage of the VAFI approach compared to the multiple TR method is much shorter data acquisition times, which are minimized when using a single SPGR measurement to augment the standard dual- TR AFI scan.

Similar to VAFI, DESPOT1-HIFI (24) is a variation on the SPGR sequence, which also utilizes simultaneous fitting to map FA and T_1 . To generate unique information to fit for an additional FA parameter, DESPOT1-HIFI utilizes an inversion pulse prior to SPGR readout. Both VAFI and DESPOT1-HIFI require some assumptions about RF pulse properties. In the case of DESPOT1-HIFI, it is assumed that the adiabatic inversion pulse is completely insensitive to any parameters affecting the spin system (B_0 , B_1 , T_1), which requires careful pulse sequence design. In VAFI, it is assumed that the pulse FA scales linearly with transmit field. Previous work (35) has shown that FA linearity is a valid assumption over the range of values herein investigated. DESPOT1-HIFI may be more time efficient than VAFI as it avoids a longer TR . However, DESPOT1-HIFI FA maps may suffer from decreased accuracy in areas with long T_1 (e.g., CSF, edema, or T_1 “black hole” lesions in multiple sclerosis). As noted in (24), these problems can be resolved through the acquisition of additional SPGR FAs and inversion recovery-SPGR inversion times tuned specifically for the longer T_1 , which would increase overall scan time of DESPOT1-HIFI accordingly. Another potential concern is the reduction of signal in DESPOT1-HIFI due to magnetization inversion. A detailed comparison of both techniques, including their SNR efficiency, is a subject of a future work.

We demonstrated that, with properly tuned parameters (proper choice of AFI and SPGR FA, phase increment of RF spoiling, and spoiler gradient area for the tissue of interest), the accuracy and precision of VAFI fit can surpass that of the standard VFA fit (when used with AFI for FA calibration) (Fig. 1). This is true even when

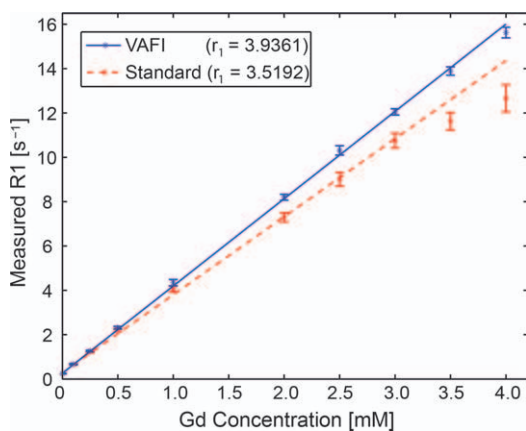


FIG. 6. Plot of R_1 vs. gadolinium concentration for the vial phantoms, using standard VFA and VAFI. The standard method shows a significant underestimation of R_1 at short T_1 times (due to errors in the AFI FA map propagating into the T_1 estimate) and the relaxivity of Gd-BOPTA. [Color figure can be viewed in the online issue, which is available at wileyonlinelibrary.com.]

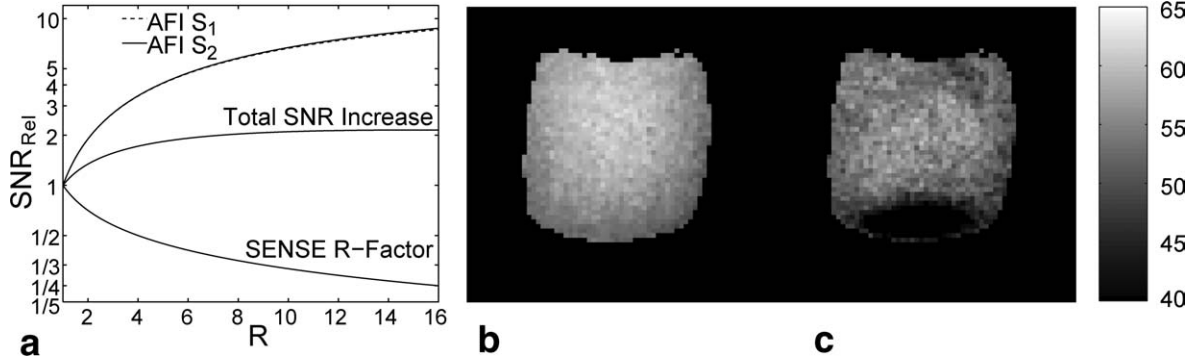


FIG. 7. **a**: Effect of SENSE on the SNR of the AFI sequence when simultaneously increasing reduction factor R and TR . Losses due to coil geometry (g -factor) were not considered. **b**: Flip angle map acquired with AFI in strong spoiling regime (long TR) for SENSE acceleration factor $R = 3$. **c**: Flip angle map acquired with AFI in weak spoiling (short TR) regime. Standard deviation of FA measurements are 11.43 and 18.21, respectively, for (b, c), and scan times are equivalent.

one SPGR measurement is eliminated, further increasing the overall time efficiency of the technique. This improvement comes from the explicit utilization of least squares estimation for solving Eq. 9, a benefit which is not available with linearized calculation of the FA and T_1 in the standard AFI and VFA methods. However, this improvement is at the cost of longer processing times than those required for original AFI and VFA approaches. An alternative and potentially faster minimization approach is to solve VAFI Eq. 5 through interleaved estimations of FA by AFI and T_1 maps by VFA (43). However, this approach obviously requires a full set of SPGR measurements to allow a separate VFA fit, and its convergence and noise performance have yet to be studied. Image reconstruction can be easily performed after data acquisition, similar to the majority of quantitative parameter mapping methods. The current implementation uses a brute-force optimization method, and as a result the algorithm requires lengthy processing times (~ 42 milliseconds per voxel or about 6 h for a high-resolution whole-brain dataset). An important next step will be to substantially reduce this time through the use of more efficient optimization methods utilizing a C-code implementation or commodity graphics processing unit hardware (44). An additional speed up is expected from initi-

alizing the algorithm using T_1 /FA values from the regular VFA/AFI fitting procedures.

A major advantage of the traditional VFA technique is the ease with which acquisition settings can be optimized, either for a single T_1 time using a pair of “ideal” FAs (33) or using sets of combined ideal angles to image over a wide range of T_1 (10). Our simulation results show that VAFI can be similarly optimized through the proper choice of FA for the proton-density-weighted SPGR measurement. Because of the nonlinear nature of VAFI, we found this optimal angle through a numerical solution instead of an empirical formula. It is important to note that the optimal choice of this FA for VAFI is neither the Ernst angle nor the same as the smallest ideal angle for a VFA experiment. However, we observed that the optimal SPGR FA is always close (within 1°) to the smallest of the “ideal” angles optimizing VFA experiment design (33). Therefore, the “ideal” angle formula may still be utilized as a close approximation to the optimal VAFI SPGR FA when designing experiments. Simulations also showed that VAFI with multiple SPGR FAs will result in improved efficiency in the wider T_1 range, similar to VFA T_1 mapping with optimized experiment designs (39,45).

A major limitation of both AFI and VFA is the need for proper spoiling parameters to ensure accurate

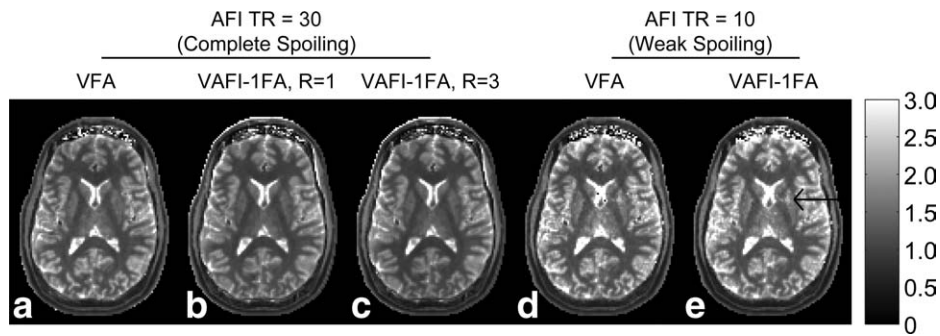


FIG. 8. In vivo T_1 maps in units of seconds in a healthy human volunteer comparing nearly complete AFI spoiling (**a–c**) versus weak spoiling (**d, e**) using standard VFA versus single flip angle VAFI techniques. For a well-spoiled sequence, both VFA and VAFI produce T_1 maps of comparable quality (see Table 2 for region of interest measurements), even though VAFI uses one less SPGR acquisition. Accelerated VAFI demonstrates similar image quality (**c**). The result of a poorly spoiled AFI sequence is visibly elevated T_1 estimates. This is even worse in the case of VAFI, where inconsistent signal levels between the AFI and SPGR datasets produce visible artifacts near the center of the image (arrow in **e**).

Table 2

Region of Interest Measurements of T_1 , Comparing Well-Spoiled Versus Poorly Spoiled AFI Using the VFA and VAFI Techniques, and Literature Values

	Weakly spoiled AFI ($TR_1 = 10$ ms)		Completely spoiled AFI ($TR_1 = 30$ ms)			Literature
	VFA	VAFI	VFA	VAFI ($R = 1$)	VAFI ($R = 3$)	
CSF	6.653 ± 1.986	5.285 ± 1.483	5.328 ± 1.645	3.944 ± 0.767	3.649 ± 0.674	4.163 ± 0.26341
WM CC genu	1.094 ± 0.066	1.215 ± 0.085	0.918 ± 0.036	0.919 ± 0.035	0.897 ± 0.038	0.99040
WM CC splenium	1.150 ± 0.044	1.167 ± 0.071	1.068 ± 0.045	0.966 ± 0.038	0.930 ± 0.050	1.02040
WM frontal	1.068 ± 0.050	1.163 ± 0.057	0.992 ± 0.023	1.004 ± 0.023	0.976 ± 0.027	0.94040
WM internal cap	1.169 ± 0.050	1.168 ± 0.047	1.031 ± 0.047	0.963 ± 0.035	0.985 ± 0.036	0.98040
GM caudate	1.818 ± 0.132	1.982 ± 0.177	1.505 ± 0.071	1.535 ± 0.085	1.480 ± 0.100	1.41040
GM putamen	1.676 ± 0.145	1.704 ± 0.171	1.470 ± 0.086	1.372 ± 0.076	1.368 ± 0.082	1.33040
GM thalamus	1.744 ± 0.101	1.740 ± 0.104	1.446 ± 0.095	1.344 ± 0.094	1.336 ± 0.108	1.22040

quantification (27). Although strong AFI spoiling is still a necessity for VAFI, simulations and *in vivo* studies have shown that the need for strong SPGR spoiling in the case of VAFI may be greatly reduced if a single FA SPGR measurement is used. This may allow reduction of spoiling gradients for SPGR part of VAFI and, as a result, more time-efficient overall mapping of the FA and T_1 than that is available with AFI and VFA alone. Notably, the dependence of T_1 accuracy on the choice of RF phase increment becomes much smaller. This is similar to a previous modification of the VFA method, which proposed an SPGR RF phase increment near the plateau of the curve rather than near a zero crossing in order to reduce the sensitivity of T_1 to this value (46). However, the previous method requires an additional correction to the subsequent T_1 maps, which is not necessary in VAFI.

One must consider the time efficiency of VAFI compared to the traditional VFA and AFI approaches when used separately. In the context of T_1 -insensitive FA mapping, VAFI requires a short TR SPGR acquisition in addition to AFI, which may increase the overall scan time insignificantly (by 6% in our unaccelerated version compared to standard AFI scan time). In the context of T_1 mapping, VAFI requires that both the AFI and SPGR scans be matched in spatial resolution, at the resolution of interest for T_1 mapping. Although this eliminates the need for one SPGR measurement without a loss of precision, an AFI scan with the optimal $n = TR_{AFI2}/TR_{AFI1} = 5$ is six times longer than a normal SPGR acquisition, which may make straightforward high resolution (~ 1 mm³) T_1 mapping with VAFI less efficient than with alternative VFA-based T_1 mapping techniques (24). Although such full resolution VAFI may potentially improve accuracy of FA/ T_1 mapping if there is a partial volume effect between very short (problematic AFI regime) and long T_1 components, several options may help minimize imaging times and simultaneously maintain accurate FA/ T_1 mapping with VAFI. One approach is to acquire an AFI dataset at a lower spatial resolution along with a standard VFA acquisition of two SPGR images at the desired resolution and to use low-resolution VAFI to fit for FA. Such method would still benefit from high accuracy due to proper spoiling and T_1 independence of FA maps, but would not benefit from a reduced number

of VFA SPGR measurements and a gain in T_1 precision from simultaneous least squares fitting. As we confirmed in this article, parallel imaging is also a very suitable option for acceleration of VAFI, as the signal boost from longer AFI TR efficiently compensates SNR losses from parallel MRI (38), an effect mostly unavailable for inherently short TR techniques (24). Parallel MRI was used to accelerate AFI ($R = 3$) resulting in the acquisition of a VAFI T_1 mapping in under 5 min with a minimal effect on the map quality and accuracy ($<3.6\%$ error in WM/GM T_1). The method can be further accelerated for increased coverage or higher resolution imaging using systems with larger numbers of receive channels or lower resolution VAFI mapping as discussed above. The other recommended parameters for AFI part of *in vivo* protocol are $TR_{AFI1} = 30$ ms, $TR_{AFI2} = 150$ ms, $\alpha_{AFI} = 55^\circ$, $A_{G1} = 450$ mT*ms/m, $\phi_0 = 44^\circ$, and a SENSE acceleration factor of 3. Recommended SPGR parameters are $TR = 10$ ms, $\alpha_{SPGR} = 3^\circ$, $A_G = 38$ mT*ms/m, and $\phi_0 = 30^\circ$.

CONCLUSION

The VFA method is a rapid and accurate method for measuring T_1 , as long as it can be paired with an equally rapid and accurate method for measuring and correcting FA. In this study, we presented a method that combines VFA and AFI into a single procedure, named VAFI. This allows the TR of the AFI sequence to be extended to accommodate a large spoiler gradient for proper quantification, while removing the main AFI requirement of $TR_{AFI1,2} \ll T_1$. We showed in both Monte Carlo simulations and phantom scans that this method is highly accurate at estimating both FA and T_1 in the presence of very short T_1 times, with greater precision than the traditional VFA approach. We showed in simulations and *in vivo* scans that proper spoiling of the AFI sequence is essential to accurate quantification, while the spoiling requirements of the SPGR portion of the experiment are considerably reduced, resulting in a much shorter SPGR acquisition time. The proposed VAFI method has a high potential to become a widely used T_1 /FA mapping approach in a variety of high-field imaging applications, particularly those with shortened T_1 values such as dynamic contrast-enhanced perfusion MRI.

ACKNOWLEDGMENTS

The authors thank Dr. Alex Frydrychowicz and Dr. Ian Rowland for assistance with phantom experiments.

REFERENCES

- Pykett IL, Rosen BR, Buonanno FS, Brady TJ. Measurement of spin-lattice relaxation times in nuclear magnetic resonance imaging. *Phys Med Biol* 1983;28:723–729.
- Look DC, Locker DR. Time saving in measurement of NMR and EPR relaxation times. *Rev Sci Instrum* 1970;41:250–251.
- Shah NJ, Zaitsev M, Steinhoff S, Zilles K. A new method for fast multislice T(1) mapping. *Neuroimage* 2001;14:1175–1185.
- Deichmann R. Fast high-resolution T1 mapping of the human brain. *Magn Reson Med* 2005;54:20–27.
- Henderson E, McKinnon G, Lee TY, Rutt BK. A fast 3D look-locker method for volumetric T1 mapping. *Magn Reson Imaging* 1999;17:1163–1171.
- Christensen KA, Grant DM, Schulman EM, Walling C. Optimal determination of relaxation times of fourier transform nuclear magnetic resonance. Determination of spin-lattice relaxation times in chemically polarized species. *J Phys Chem* 1974;78:1971–1977.
- Homer J, Beevers MS. Driven-equilibrium single-pulse observation of T1 relaxation—a reevaluation of a rapid new method for determining NMR spin-lattice relaxation-times. *J Magn Reson* 1985;63:287–297.
- Fram EK, Herfkens RJ, Johnson GA, Glover GH, Karis JP, Shimakawa A, Perkins TG, Pelc NJ. Rapid calculation of T1 using variable flip angle gradient refocused imaging. *Magn Reson Imaging* 1987;5:201–208.
- Deoni SC, Peters TM, Rutt BK. High-resolution T1 and T2 mapping of the brain in a clinically acceptable time with DESPOT1 and DESPOT2. *Magn Reson Med* 2005;53:237–241.
- Cheng HL, Wright GA. Rapid high-resolution T(1) mapping by variable flip angles: accurate and precise measurements in the presence of radiofrequency field inhomogeneity. *Magn Reson Med* 2006;55:566–574.
- Gowland P, Mansfield P. Accurate measurement of T1 *in vivo* in less than 3 seconds using echo-planar imaging. *Magn Reson Med* 1993;30:351–354.
- Ordidge RJ, Gibbs P, Chapman B, Stehling MK, Mansfield P. High-speed multislice T1 mapping using inversion-recovery echo-planar imaging. *Magn Reson Med* 1990;16:238–245.
- Venkatesan R, Lin W, Haacke EM. Accurate determination of spin-density and T1 in the presence of RF-field inhomogeneities and flip-angle miscalibration. *Magn Reson Med* 1998;40:592–602.
- Collins CM, Li S, Smith MB. SAR and B1 field distributions in a heterogeneous human head model within a birdcage coil. Specific energy absorption rate. *Magn Reson Med* 1998;40:847–856.
- Insko E, Bolinger L. Mapping of the radiofrequency field. *J Magn Reson Ser A* 1993;103:82–85.
- Cunningham CH, Pauly JM, Nayak KS. Saturated double-angle method for rapid B1+ mapping. *Magn Reson Med* 2006;55:1326–1333.
- Stollberger R, Wach P. Imaging of the active B1 field *in vivo*. *Magn Reson Med* 1996;35:246–251.
- Morrell GR. A phase-sensitive method of flip angle mapping. *Magn Reson Med* 2008;60:889–894.
- Jiru F, Klose U. Fast 3D radiofrequency field mapping using echo-planar imaging. *Magn Reson Med* 2006;56:1375–1379.
- Wang D, Zuehlisdorff S, Larson AC. Rapid 3D radiofrequency field mapping using catalyzed double-angle method. *NMR Biomed* 2009;22:882–890.
- Dowell NG, Tofts PS. Fast, accurate, and precise mapping of the RF field *in vivo* using the 180 degrees signal null. *Magn Reson Med* 2007;58:622–630.
- Chavez S, Stanis G. A simple and fast flip angle calibration method. In: Annual Meeting of ISMRM, Honolulu, Hawaii, 2009. p375.
- Sacolick LI, Wiesinger F, Hancu I, Vogel MW. B1 mapping by Bloch-Siegert shift. *Magn Reson Med* 2010;63:1315–1322.
- Deoni SC. High-resolution T1 mapping of the brain at 3T with driven equilibrium single pulse observation of T1 with high-speed incorporation of RF field inhomogeneities (DESPOT1-HIFI). *J Magn Reson Imaging* 2007;26:1106–1111.
- Yarnykh VL. Actual flip-angle imaging in the pulsed steady state: a method for rapid three-dimensional mapping of the transmitted radiofrequency field. *Magn Reson Med* 2007;57:192–200.
- Wang J, Mao W, Qiu M, Smith MB, Constable RT. Factors influencing flip angle mapping in MRI: RF pulse shape, slice-select gradients, off-resonance excitation, and B0 inhomogeneities. *Magn Reson Med* 2006;56:463–468.
- Yarnykh VL. Optimal radiofrequency and gradient spoiling for improved accuracy of T1 and B1 measurements using fast steady-state techniques. *Magn Reson Med* 2010;63:1610–1626.
- Yarnykh VL. Improved accuracy of variable flip angle T1 measurements using optimal radiofrequency and gradient spoiling. In: Annual Meeting of ISMRM, Toronto, Canada, 2008. p234.
- Thuen M, Olsen O, Berry M, Pedersen TB, Kristoffersen A, Haraldseth O, Sandvig A, Brekken C. Combination of Mn(2+)-enhanced and diffusion tensor MR imaging gives complementary information about injury and regeneration in the adult rat optic nerve. *J Magn Reson Imaging* 2009;29:39–51.
- Cheng HL. T1 measurement of flowing blood and arterial input function determination for quantitative 3D T1-weighted DCE-MRI. *J Magn Reson Imaging* 2007;25:1073–1078.
- Treier R, Steingoetter A, Fried M, Schwizer W, Boesiger P. Optimized and combined T1 and B1 mapping technique for fast and accurate T1 quantification in contrast-enhanced abdominal MRI. *Magn Reson Med* 2007;57:568–576.
- Hurley SA, Samsonov AA. Accurate and efficient mapping of flip angle and T1 using simultaneous actual flip angle-variable Flip angle imaging (AFI-T1). In: Annual Meeting of ISMRM, Honolulu, Hawaii, 2009. p4450.
- Deoni SC, Rutt BK, Peters TM. Rapid combined T1 and T2 mapping using gradient recalled acquisition in the steady state. *Magn Reson Med* 2003;49:515–526.
- Chang LC, Koay CG, Basser PJ, Pierpaoli C. Linear least-squares method for unbiased estimation of T1 from SPGR signals. *Magn Reson Med* 2008;60:496–501.
- Deoni SC. Correction of main and transmit magnetic field (B0 and B1) inhomogeneity effects in multicomponent-driven equilibrium single-pulse observation of T1 and T2. *Magn Reson Med* 2011;65:1021–1035.
- Huh W, Fessler JA, Samsonov AA. Water-fat decomposition with regularized field map. In: Annual Meeting of ISMRM, Miami, Florida, 2005.
- Pruessmann KP, Weiger M, Scheidegger MB, Boesiger P. SENSE: sensitivity encoding for fast MRI. *Magn Reson Med* 1999;42:952–962.
- Weiger M, Boesiger P, Hilfiker PR, Weishaupt D, Pruessmann KP. Sensitivity encoding as a means of enhancing the SNR efficiency in steady-state MRI. *Magn Reson Med* 2005;53:177–185.
- Deoni SC, Peters TM, Rutt BK. Determination of optimal angles for variable nutation proton magnetic spin-lattice, T1, and spin-spin, T2, relaxation times measurement. *Magn Reson Med* 2004;51:194–199.
- Underhill HR, Yuan C, Yarnykh VL. Direct quantitative comparison between cross-relaxation imaging and diffusion tensor imaging of the human brain at 3.0 T. *Neuroimage* 2009;47:1568–1578.
- Lin C, Bernstein M, Huston J, Fain S. Measurements of T1 relaxation times at 3.0T: implications for clinical MRA. In: Annual Meeting of ISMRM, Glasgow, Scotland, 2001. p1391.
- Voigt T, Nehrke K, Doessel O, Katscher U. T1 corrected B1 mapping using multi-TR gradient echo sequences. *Magn Reson Med* 2010;64:725–733.
- Xue Y, Rosen MA, Song H. Improved T1 mapping with iterative actual flip-angle imaging (iAFI) technique. In: Annual Meeting of ISMRM, Stockholm, Sweden, 2010. p1722.
- Wang D, Shi L, Wang YX, Yuan J, Yeung DK, King AD, Ahuja AT, Heng PA. Concatenated and parallel optimization for the estimation of T1 map in FLASH MRI with multiple flip angles. *Magn Reson Med* 2010;63:1431–1436.
- Samsonov AA, Alexander AL, Jung Y, Field AS. Practical optimum experimental designs for fast T1 relaxometry with SPGR sequences. In: Proceedings of ISMRM, Toronto, 2008. p3081.
- Preibisch C, Deichmann R. Influence of RF spoiling on the stability and accuracy of T1 mapping based on spoiled FLASH with varying flip angles. *Magn Reson Med* 2009;61:125–135.

Analysis and Correction of Biases in Cross-Relaxation MRI due to Biexponential Longitudinal Relaxation

Pouria Mossahebi,¹ Vasily L. Yarnykh,² and Alexey Samsonov^{3*}

Purpose: Cross-relaxation imaging (CRI) is a family of quantitative magnetization transfer techniques that utilize images obtained with off-resonance saturation and longitudinal relaxation rate (R_1) maps reconstructed by the variable flip angle (VFA) method. It was demonstrated recently that a significant bias in an apparent VFA R_1 estimation occurs in macromolecule-rich tissues due to magnetization transfer (MT)-induced biexponential behavior of longitudinal relaxation of water protons. The purpose of this article is to characterize theoretically and experimentally the resulting bias in the CRI maps and propose methods to correct it.

Theory: The modified CRI algorithm is proposed, which corrects for such biases and yields accurate parametric bound pool fraction f , cross-relaxation rate k , and R_1 maps. Additionally, an analytical correction procedure is introduced to recalculate previously obtained parameter values.

Results: The systematic errors due to unaccounted MT-induced biexponential relaxation can be characterized as an overestimation of R_1 , f , and k , with a relative bias comparable with the magnitude of f . The phantom and human in vivo experiments demonstrate that both proposed modified CRI and analytical correction approaches significantly improve the accuracy of the CRI method.

Conclusion: The accuracy of the CRI method can be considerably improved by taking into account the contribution of MT-induced biexponential longitudinal relaxation into variable flip angle R_1 measurements. **Magn Reson Med 71:830–838, 2014.**

© 2013 Wiley Periodicals, Inc.

Key words: magnetization transfer; two-pool model; cross-relaxation imaging; variable flip angle T_1 mapping

Magnetization transfer (MT) effect is commonly recognized as a source of important information about tissue microstructure due to its sensitivity to immobile macromolecular protons not detectable by the conventional MRI (e.g., those associated with proteins and lipid bilayers of myelin, collagen matrix in cartilage, muscle fibers, etc.)

(1,2). Various approaches have been proposed to quantify the MT effect in vivo including empirical indexes characterizing signal saturation due to MT (1,3,4) and methods for quantitative mapping of specific parameters describing MT within the two-pool model (2,5–15). The key parameters of interest in this model are associated with the state of macromolecular protons, which is characterized by their molar fraction (bound pool fraction, f), the forward rate constant describing cross-relaxation with water protons (k), and the transverse relaxation time T_2^B . Particularly promising findings were reported for the bound pool fraction, which was found to be correlated with the myelin content in neural tissues (16–19) and was shown to be capable of tracking age-related changes of the white matter (WM) myelination in animal studies (20).

One group of quantitative MT methods termed cross-relaxation imaging (CRI) (6,10,12) is specifically targeted at mapping the parameters f , k , and T_2^B or their subsets in the isolation from relaxation properties of the water proton magnetization. Collectively, these techniques rely on the approximate two-pool pulsed MT formalism (6,10) where the action of off-resonance saturation pulses on the macromolecular proton pool is described by an effective time-independent saturation rate calculated for a square pulse with the equivalent power and duration. Further, direct saturation of the free water proton pool is either neglected (6) or estimated within the stationary approximation sufficiently far from the resonance (10). These techniques allow three-dimensional (3D) acquisition with clinically acceptable scan times and resolution based on a limited number of MT-weighted images obtained with variable off-resonance saturation. The common feature of CRI and other off-resonance qMT techniques is the need for complementary T_1 mapping, which allows decoupling of the two-pool model parameters from the longitudinal relaxation rate $R_1 = 1/T_1$ (5–7,9,10,12). Because of the need for the fast 3D acquisition, T_1 maps are often generated using the variable flip angle (VFA) method with a spoiled gradient-echo (SPGR) sequence (21). It has been realized recently that the VFA method originally derived for the single-pool model inaccurately describes the SPGR signal, which often leads to biased R_1 estimation in tissues with rich macromolecular content. This bias is due to unaccounted cross-relaxation caused by MT effect between macromolecular and water protons, which leads to the biexponential behavior of longitudinal relaxation of water proton magnetization in such tissues (22). The cross-relaxation contribution was shown to dominate R_1 of water in hydrated collagen (22) and more recently in neural tissues (23). Deviation of longitudinal

¹Department of Biomedical Engineering, University of Wisconsin-Madison, Madison, Wisconsin, USA.

²Department of Radiology, University of Washington, Seattle, Washington, USA.

³Department of Radiology, University of Wisconsin-Madison, Madison, Wisconsin, USA.

Grant sponsor: NIH NINDS; Grant number: R01NS065034. Grant sponsor: NIBIB; Grant number: R21EB009908.

*Correspondence to: Alexey Samsonov, Ph.D., Department of Radiology, University of Wisconsin-Madison, WIMR, 1111 Highland Dr, Rm. 1117, Madison, WI 53705. E-mail: samsonov@wisc.edu

Received 19 October 2012; revised 28 December 2012; accepted 14 January 2013

DOI 10.1002/mrm.24677

Published online 25 February 2013 in Wiley Online Library (wileyonlinelibrary.com).

© 2013 Wiley Periodicals, Inc.

relaxation from a single-exponential behavior due to cross-relaxation significantly affects signal intensities in the fast gradient-echo sequences (24,25) and introduces a bias in VFA R_1 measurements that depends on the pulse sequence parameters and may reach up to 14–15% in brain WM (24).

Apart from biasing VFA R_1 estimation, systematic errors from unaccounted biexponential relaxation may further propagate into the two-pool model parameters estimated by quantitative MT techniques such as CRI. Conversely, an unbiased determination of R_1 values in tissues requires the knowledge about the rest of parameters of the two-pool model, which may not be practical for data correction within the VFA method alone (24). In this study, we propose the unified treatment of VFA and MT SPGR signals using a modified CRI (mCRI) analysis, which enables simultaneous corrections of R_1 and two-pool MT model parameters. In particular, we theoretically and experimentally characterize systematic errors in CRI caused by biexponential relaxation in VFA R_1 mapping and demonstrate a new processing algorithm, which corrects for such errors and yields accurate parametric f , k , T_2^B , and R_1 maps. Additionally, we propose an analytical correction procedure allowing recalculation of previously obtained cross-relaxation parameter values with acceptable residual errors.

THEORY

Analytical Theory of the SPGR Signal in the Presence of Cross-Relaxation

To estimate the effect of cross-relaxation on the apparent R_1 measured by the VFA method, we employ the previously described pulsed steady-state formalism (6,10) in the simplified form, where no off-resonance saturation is applied. The matrix model of the longitudinal magnetization (based on Eq. [1] in Ref. 10) can be rewritten as:

$$\mathbf{M}_z = (\mathbf{I} - \mathbf{E}\mathbf{C})^{-1}(\mathbf{I} - \mathbf{E})\mathbf{M}_{eq}, \quad [1]$$

where $\mathbf{M}_z = [M_z^F \ M_z^B]^T$ corresponds to the longitudinal magnetization before the excitation pulse, M_z^F , M_z^B are the longitudinal magnetizations of free and bound protons, respectively, $\mathbf{M}_{eq} = \mathbf{M}_0[1-f \ f]^T$ is the vector of equilibrium magnetization, \mathbf{I} is the identity matrix, the matrix $\mathbf{E} = \exp(\mathbf{R}T_R)$ describes relaxation during repetition time T_R , and the diagonal matrix $\mathbf{C} = \text{diag}(S_f, S_b)$, $S_f = \cos \alpha$, $S_b = 1$ corresponds to the instant rotation of the magnetization M_z^F by an excitation pulse with the flip angle α . The relaxation matrix \mathbf{R} is defined as follows:

$$\mathbf{R} = \begin{bmatrix} -R_1^F - k & k \frac{1-f}{f} \\ k & -R_1^B - k \frac{1-f}{f} \end{bmatrix} \quad [2]$$

where R_1^F and R_1^B are the longitudinal relaxation rates of the free and bound pool, respectively. Applying the first-order approximation to the exponential terms, Eq. [1] can be simplified to

$$\mathbf{M}_z \approx (\mathbf{R}T_R + \ln \mathbf{C})^{-1} \mathbf{R} \mathbf{M}_{eq} T_R \quad [3]$$

Corresponding approximated expression for the observed signal can be explicitly written as follows:

$$S \approx \frac{M_0(1-f)(R_1^F R_1^B + R_1^F k(1-f)/f + R_1^B k) \sin \alpha \exp(-T_E/T_2^*)}{R_1^F R_1^B + R_1^F k(1-f)/f + R_1^B + k - (R_1^B + k(1-f)/f) T_R^{-1} \ln(\cos \alpha)} \quad [4]$$

We further assume that $R_1^F = R_1^B = R_1$ similar to earlier studies (6,12) that corresponds to the fast exchange conditions (26). With these assumptions, the signal intensity is expressed as:

$$S \approx \frac{M_0(1-f)R_1 T_R \sin \alpha \exp(-T_E/T_2^*)}{R_1 T_R - \ln(\cos \alpha) + \frac{k \ln(\cos \alpha)}{R_1 + k/f}} \quad [5]$$

Finally, the relaxation rate R_1 can be neglected in the sum with a much larger term k/f , thus providing the signal equation

$$S \approx M_0(1-f) \frac{R_1 T_R}{R_1 T_R - (1-f) \ln(\cos \alpha)} \sin \alpha \exp(-T_E/T_2^*) \quad [6]$$

By comparing Eq. [6] with the first-order approximation of the Ernst equation (27) (not shown for brevity), the relationship between the true R_1 and its apparent value R_1^{app} estimated from VFA data becomes evident:

$$R_1^{\text{app}} \approx R_1 / (1-f) \quad [7]$$

Equation [7] demonstrates that the bias in R_1 caused by cross-relaxation is on the order of f and independent of the sequence parameters (T_R and flip angles) if the first-order approximation is justified by a short T_R . More general treatment for arbitrary sequence parameters can be found in Ref. 24 and 25.

Effect of Apparent R_1 on the CRI Parameters

The next goal is to estimate systematic errors in the two-pool model parameters due to R_1^{app} in the CRI method. We start our analysis with a simplified CRI model (6), which allows analytical investigation of errors in the estimated parameters in the regime where the direct saturation effect is negligible ($\Delta > 2.5$ kHz) (28). According to this model, the ratio of signals with and without off-resonance saturation in a pulsed MT experiment can be expressed as

$$\frac{M_z^F(W^B)}{M_z^F(W^B=0)} \approx \frac{P + (Q-1)sW^B}{P + QsW^B} \quad [8]$$

where

$$P = f^{-1}(R_1 - (1-f)T_R^{-1} \ln(\cos \alpha)) \quad [9]$$

$$Q = k^{-1}(R_1 - T_R^{-1} \ln(\cos \alpha)) + 1 \quad [10]$$

and W^B is the saturation rate of the bound pool scaled by the duty cycle of the saturation pulse ($s = t_{\text{mt}}/T_R$,

where t_{mt} is the pulse duration). The saturation rate W^B depends on the offset frequency and the flip angle of the saturation pulse and is determined by the parameter T_2^B based on an appropriate spectral line shape model [typically SuperLorentzian (29)]. If the data are fitted in the form given by Eq. [8], the fitting algorithm searches for the optimal parameters P , Q , and T_2^B regardless of an actual R_1 .

The effect of R_1 errors on the two-pool model parameters originates from the dependence of the coefficients P and Q on R_1 (Eqs. [9] and [10]). Accordingly, if R_1^{app} is supplied as input information, apparent values f^{app} and k^{app} will be obtained. The relationships between the true f and k and their apparent values can be derived from the conditions $P(R_1^{app}, f^{app}) = P(R_1, f)$ and $Q(R_1^{app}, k^{app}) = Q(R_1, k)$, which result in the simple recalculation formulas:

$$f = Cf^{app}, \quad k = Ck^{app} \quad [11]$$

where the correction coefficient C is the same for both f and k and depends on T_R and the flip angle:

$$C = (R_1^{app} - T_R^{-1} \ln(\cos \alpha)) / (R_1^{app} - T_R^{-1} \ln(\cos \alpha) + f^{app} R_1^{app}) \quad [12]$$

The above analysis also suggests that R_1 errors should not affect T_2^B , since W^B is independent of R_1 (6). We refer below to the recalculation formulas (Eqs. [11] and [12]) as CRI with the first-order correction.

Standard CRI and mCRI Approaches

In the original CRI approach (10), reconstruction of parametric maps is performed in two stages (Fig. 1). During the first stage, R_1 map is calculated by fitting the Ernst equation to VFA SPGR data (21). During the second step, the matrix model of the pulsed MT is fitted to MT-weighted data, while R_1 is supplied as an external parameter. Prior to the fit, the MT data are normalized pixel-

wise by an arbitrary reference image typically obtained without saturation. The purpose of this normalization is to reduce the number of free parameters in the fit by excluding a multiplicative factor commonly referred to as proton density, which absorbs the effects of spin concentration, T_2^* decay, and the coil sensitivity. The normalized data are then fitted to the corresponding ratio of analytical signal expressions with and without saturation $M_z^F(W^B)/M_z^F(W^B=0)$. As an alternative to the standard CRI approach, we propose the mCRI reconstruction algorithm to perform a global fit of VFA and MT SPGR data simultaneously (Fig. 1). On the first stage, similarly to the standard CRI approach, the normalization procedure is uniformly applied to both VFA and MT data to exclude the common proton density term. Then, the normalized images are simultaneously fitted to the corresponding ratios of analytical signal expressions with and without saturation using Eq. [1] from this paper and Eq. [1] from Ref. 10, respectively. Accordingly, the global fit simultaneously yields all the remaining parameters (R_1 , f , k , T_2^B) and automatically takes into account the cross-relaxation contribution into VFA data (Fig. 1).

METHODS

Simulations

To estimate errors in the two-pool model parameters caused by the unaccounted biexponential relaxation, synthetic VFA and MT SPGR signal intensities were generated using Eq. [1] from this paper and Eq. [1] from Ref. 10, respectively. Then, datasets were fitted using the original CRI algorithm. The first-order correction formulas (Eqs. [7], [11], and [12]) were also evaluated. Specific parameters used in the simulations were taken from regions-of-interest (ROI) measurements in the genu of corpus callosum (WM) and thalamus (GM) from full mCRI fit of the in vivo data presented below: 1) WM: $R_1 = 0.97 \text{ s}^{-1}$; $f = 15.36 \%$; $k = 2.70 \text{ s}^{-1}$; $T_2^B = 9.84 \text{ } \mu\text{s}$; 2) GM: $R_1 = 0.71 \text{ s}^{-1}$; $f = 8.8\%$; $k = 1.57 \text{ s}^{-1}$; $T_2^B = 10.21 \text{ } \mu\text{s}$. To study the effect of approximations of the first order

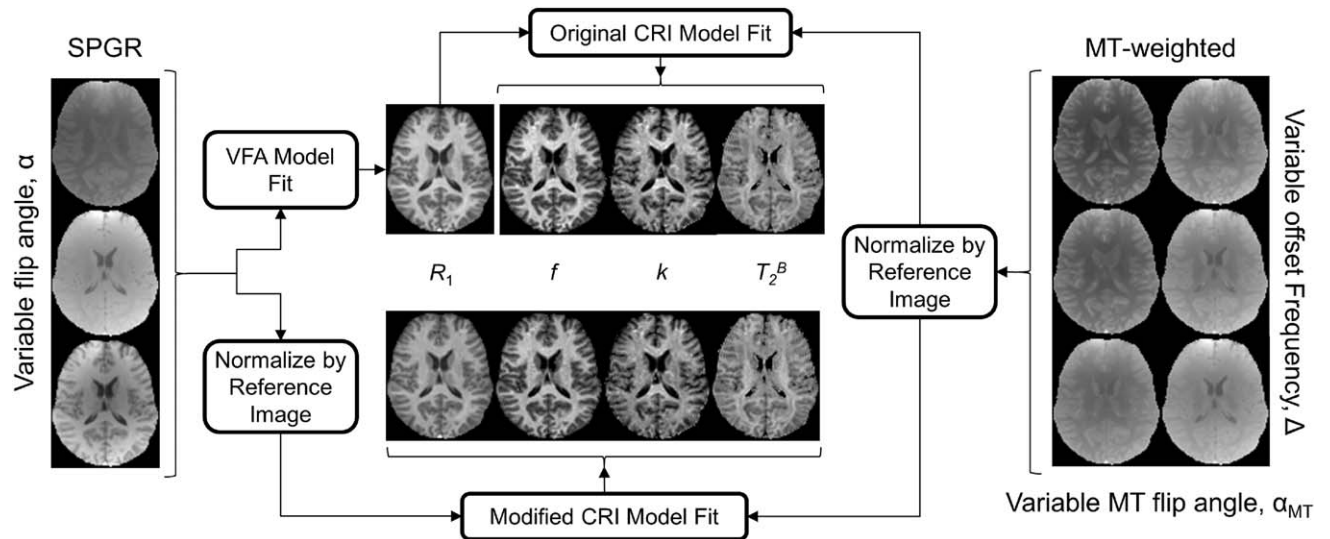


FIG. 1. Original CRI and mCRI processing pipelines.

correction in the realistic imaging regime, pulse sequence parameters and sampling scheme in these simulations corresponded to those used in the in vivo experiments detailed below.

Phantom Preparation

Five crosslinked BSA samples (98% bovine serum albumin, essentially fatty acid free, Sigma-Aldrich Corp., St. Louis, MO) were prepared with BSA percent weight of 10, 15, 20, 25, and 30 as described in Ref. 30. The BSA was dissolved in distilled water and was placed in the ice bath for 10 min. Then, 50 $\mu\text{L/mL}$ of an ice-cold 25% glutaraldehyde solution (Sigma-Aldrich Corp., St. Louis, MO) were added to the BSA solution while stirring with a syringe needle. The samples were kept at the room temperature for two hours and then stored at 4°C.

Data Acquisition

Imaging experiments were carried out on a 3.0 T GE Discovery MR750 (GE Healthcare; Waukesha, WI) using either an eight-channel transmit/receive knee coil (for phantom scans) or eight-channel phased array head coil (for a volunteer scan). All data were acquired with the 3D MT-weighted SPGR sequence in a strong spoiling regime (31) (spoiling gradient area $A_G = 450 \text{ mT}\cdot\text{ms/m}$, RF phase increment 169°). In the phantom experiment, eight Z-spectroscopic datasets were acquired ($T_R/T_E = 37/2.3 \text{ ms}$, excitation flip angle $\alpha = 15^\circ$) with the 18 ms Fermi saturation pulse applied at the offset frequencies $\Delta = 2.5, 10, 18, 26 \text{ kHz}$ with two nominal saturation flip angles $\alpha_{\text{MT}} = 850^\circ$ and 1300° . Additionally, four VFA SPGR datasets were acquired using the same sequence with $\Delta = 250 \text{ kHz}$ to ensure that the transmitter operates with identical gain settings (no MT effect is observed at this frequency) and flip angles optimized for the range of T_1 values in the phantoms ($\alpha = 6^\circ, 15^\circ, 35^\circ$, and 50°). The SPGR dataset with the highest signal-to-noise ratio ($\alpha = 15^\circ$) was used as a reference image to normalize both Z-spectroscopic and VFA data as explained in the previous section. All datasets were acquired with field of view $= 140 \times 105 \times 48 \text{ mm}^3$ and matrix $= 128 \times 96 \times 24$. Single-slice 2D inversion-prepared spin-echo (IR) data were collected to determine reference T_1 values in the phantoms ($T_R/T_E = 5000/8.2 \text{ ms}$, $T_1 = 0.3, 0.5, 0.7, 0.9, 1.2, 1.6$, and 2 s).

Informed written consent was obtained from a healthy volunteer in accordance with the local institutional policy. Eight Z-spectroscopic datasets were acquired using the same pulse sequences ($\Delta = 2.5, 5, 9, 13 \text{ kHz}$, $\alpha_{\text{MT}} = 500^\circ, 1100^\circ$, $\alpha = 10^\circ$). Four VFA datasets were acquired with flip angles $\alpha = 5^\circ, 10^\circ, 20^\circ$, and 30° . The image with $\alpha = 10^\circ$ was used as a reference dataset. All Z-spectroscopic and VFA data were acquired with $T_R/T_E = 40/2.0 \text{ ms}$, field of view $= 240 \times 180 \times 80 \text{ mm}^3$ and matrix $= 128 \times 96 \times 42$. The total scan time for this protocol was 35 min.

B_0 and B_1 maps were used to correct flip angle and local off-resonance frequency values in both phantom and volunteer studies. B_1 maps were acquired using the actual flip angle imaging method (32) ($T_{R,1}/T_{R,2}/T_E = 37/185/2.3 \text{ ms}$, $\alpha = 55^\circ$, field of view $= 240 \times 180 \times 80 \text{ mm}$, matrix $= 96 \times 72 \times 28$) with the strong spoiling regime

(31). B_0 maps were calculated from the 3D fat-water separation method known as “iterative decomposition of water and fat with echo asymmetry and least squares estimation” with field of view $= 240 \times 180 \times 80 \text{ mm}$ and matrix $= 256 \times 256 \times 42$ (33). The scan time for these additional B_0 and B_1 mapping sequences was 10 min.

Image Processing and Analysis

The standard CRI processing workflow (Fig. 1) was implemented according to (10,34). In mCRI, all parametric maps were generated by fitting the normalized VFA and MT data simultaneously as described above (Fig. 1) using in-house-written C and MATLAB (MathWorks, Natick, MA) software utilizing a standard “*lsqnonlin*” function for nonlinear least squares voxel-based fitting (<http://www.medphysics.wisc.edu/~samsonov/qmap>). All quantitative parameters estimated in the phantom scans and in vivo were obtained from parametric maps in the manually drawn ROIs.

To study the association between BSA content and the bound pool fraction determined by different processing approaches, we performed linear regression analysis using the following model:

$$f = \beta_1 * \text{BSA}\% + \beta_0 \quad [13]$$

The strength of anticipated linear relationships was assessed using the Pearson’s correlation coefficient. We additionally tested if the intercept β_0 is significantly different from zero (the anticipated value for f at $\text{BSA}\% = 0$). Statistical significance of differences between parameter measurements by CRI, mCRI, and CRI with the first-order correction was assessed using a paired two-tailed *t*-test.

RESULTS

Simulations

Table 1 shows the systematic errors in the estimated parameters in WM and GM obtained from the original CRI method, mCRI, and CRI with the first-order correction. As predicted by the theory, the R_1 bias propagates into f and k measurements but does not affect T_2^B , and it is most prominent for WM. A major portion of the biases are removed by the proposed first-order correction, with R_1 and f being corrected most efficiently ($<1\%$ residual error).

Figure 2 further illustrates the dependence of the biases on the fraction of bound protons in WM. Again, the unaccounted biexponential relaxation in the SPGR signal model introduces a substantial bias into all quantitative MT parameters except for T_2^B when estimated by

Table 1
Simulated Relative Bias in Two-Pool MT Model Parameters
Obtained by the Original CRI Fit and Its First-Order Correction
due to the Unaccounted Biexponential Relaxation for WM and GM

	Original CRI				First-order correction		
	R_1 (%)	f (%)	k (%)	T_2^B (%)	R_1 (%)	f (%)	k (%)
WM	16.92	12.42	15.20	−0.08	−0.96	−0.42	2.04
GM	8.88	5.95	6.46	−0.07	−0.64	−0.24	0.24

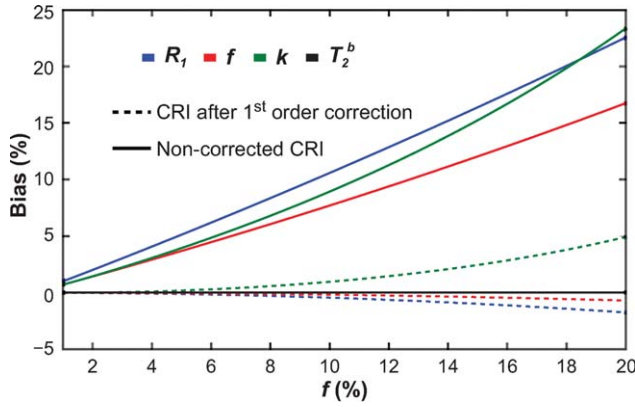


FIG. 2. Relative bias in parameters estimated using original CRI before and after first-order correction vs. bound pool fraction. The other two-pool model parameters were fixed with values corresponding to WM.

the original CRI method. These errors affect most significantly R_1 values, then k and f values. They are steadily growing with the bound pool fraction as predicted by Eqs. [7] and [11]. The first-order correction (Eqs. [11] and [12]) removes most of the bias for a wide range of f values, while the level of residual errors increases with an increase in f . The first-order correction is less accurate for k values where the residual bias may reach up to $\sim 5\%$ for tissues with a higher macromolecular content.

Phantom Studies

Figure 3 shows estimates of the two-pool MT model parameters in the BSA phantoms obtained by the original CRI, mCRI, and CRI with the first-order correction, as well as R_1 values from the reference IR experiment. Both mCRI fit and the first-order correction of CRI fit provide a good agreement with the reference IR R_1 measurements, while the standard VFA method results in substantial discrepancy with IR R_1 estimates. The difference between R_1 values measured by the VFA method and IR method increases with BSA concentration as predicted by Eq. [7] and the simulations (Fig. 2).

Similarly, the original CRI tends to overestimate bound pool fraction f and cross-relaxation rate k in the phantoms with a higher concentration of BSA. Although the first-order correction of f provides a good agreement with the mCRI fit for all concentrations, an increase in the macromolecular content leads to a poorer first-order correction for k , as predicted by the simulations (Fig. 2). T_2^b is consistent among different concentrations of BSA.

Figure 4 and Table 2 show results of a linear regression analysis of f from phantom data. The bound pool fraction strongly correlates with BSA concentration for both CRI and mCRI, though the original CRI estimation lead to a somewhat weaker correlation (Table 2). The intercept of the fitted line for mCRI and the first-order correction is not significantly different from zero, thus

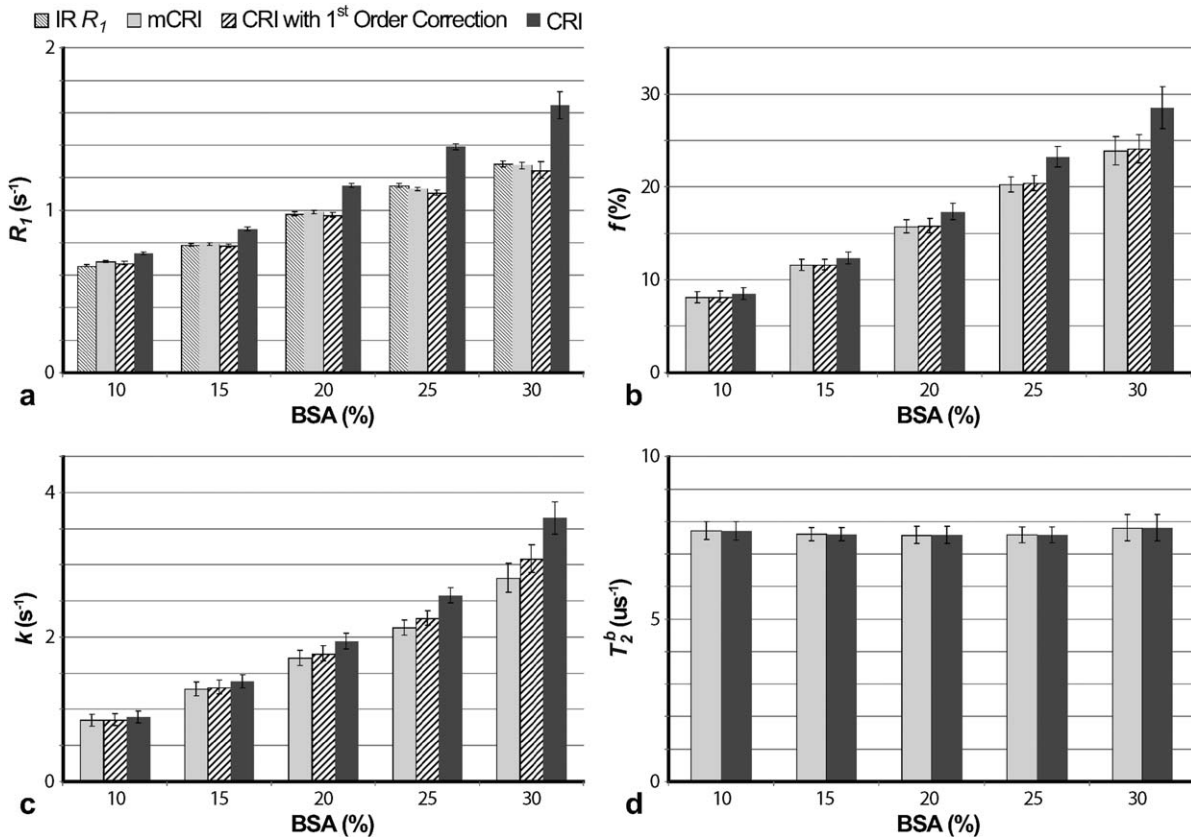


FIG. 3. Comparison of qMT parameters estimated using original CRI (without and with first-order correction) and mCRI in phantoms with different BSA concentrations. **a**: R_1 measurements. IR R_1 values are shown for reference. **b–d**: f , k , and T_2^b measurements, respectively. Error bars indicate standard deviations in ROI measurements taken from parameter maps.

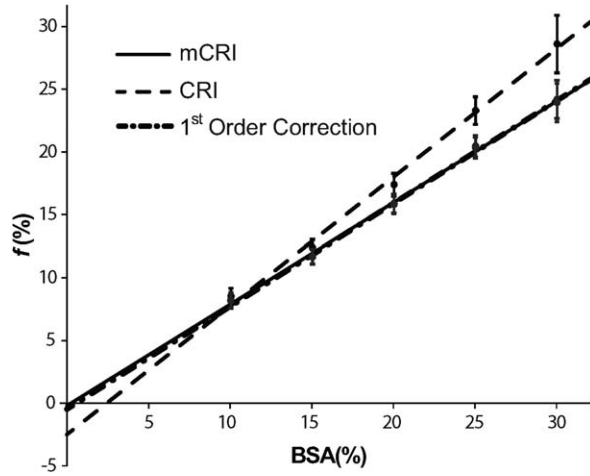


FIG. 4. Results of linear regression of bound pool fraction values derived by CRI, CRI with the first-order correction, and mCRI vs. BSA concentration. Error bars indicate standard deviations in ROI measurements taken from parameter maps.

reflecting the anticipated absence of the bound proton pool at 0% BSA concentration. At the same time, the intercept of the fitted line for original CRI is significantly different from zero and appears in the physically unrealistic range ($\sim -2.5\%$).

In Vivo Results

Figure 5 compares parametric maps obtained using the mCRI processing approach with original CRI and its first-order correction. Table 3 provides quantitative comparisons of qMT parameters in several WM and GM regions of interest. Processing with mCRI resulted in structurally similar, but quantitatively different parametric maps. For all parameters except for T_2^B , the error images reveal dependence of the bias on the macromolecular content as predicted by simulations and phantom studies. First-order correction efficiently minimizes the errors in f and R_1 . However, there is still a visible residual error for k values after the first-order correction, with most appreciable residue in WM regions, which is in agreement with simulations and phantom experiments (Figs. 2 and 3, Table 1). Statistical analysis of ROI data detected significant differences between CRI and mCRI for all parameters except for T_2^B in gray matter (Table 4). The effect of the first-order correction was also significant for R_1 , f , and k . There were significant differences between mCRI and the first-order correction for R_1 and k . These systematic errors as well as bias between mCRI and the first-order correction (Table 4) are consistent with the estimates predicted in simulations (Table 1).

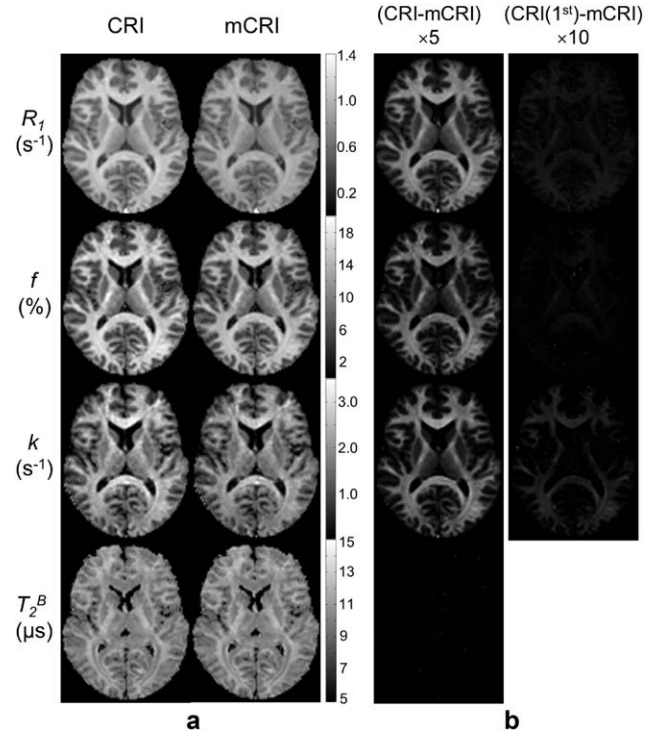


FIG. 5. Parametric MT maps estimated using original CRI and mCRI (a), and errors of the original CRI and its first-order correction [CRI (1st)] presented as difference maps with respect to mCRI (b). Note the consistency between levels of error in individual maps vs. macromolecular content as revealed by the bound pool fraction.

DISCUSSION

MT imaging offers unique sensitivity to macromolecular content in tissues that cannot be assessed with conventional MRI. Accurate modeling of MT processes using the two-pool model is essential to yield specific parameters characterizing the macromolecular fraction in both normal and pathological conditions. This study demonstrates on the example of CRI, one of qMT methods based on SPGR pulse sequence, that separate treatment of VFA and MT data may cause non-negligible systematic errors in both R_1 and quantitative MT parameters such as bound pool fraction f and cross-relaxation rate k . Specifically, this type of errors can be characterized as an overestimation of R_1 , f , and k with a relative bias comparable with magnitude of f (Fig. 2, Tables 1, 3, and 4). As the effect of the MT-induced biexponential longitudinal relaxation on the parameters estimation strongly depends on the macromolecular content in tissues (Fig. 2), the original CRI method and other qMT analysis techniques that do not take into account this effect may make interpretation of quantitative parameters

Table 2
Results of Linear Regression Analysis for Bound Pool Fraction f in BSA Phantoms

	β_0 (P-value)	β_1	R^2
CRI	$-2.46e-2 \pm 0.18e-3$ ($<10^{-4}$) [*]	$1.02e-2 \pm 8.63e-5$	0.965
First-order correction	$-0.25e-2 \pm 1.31e-3$ (0.053)	$0.81e-2 \pm 6.16e-5$	0.972
mCRI	$-0.14e-2 \pm 1.27e-3$ (0.256)	$0.80e-2 \pm 6.00e-5$	0.972

Asterisk (*) indicated that the difference between the intercept of the fitted line and zero is statistically significant.

Table 3

In Vivo Measurements of the Two-Pool MT Model Parameters Using mCRI, Original CRI, and CRI with First-Order Correction

Regions-of-interest	mCRI				Original CRI				First-order correction		
	R_1 (s ⁻¹)	f (%)	k (s ⁻¹)	T_2^B (μs)	R_1 (s ⁻¹)	f (%)	k (s ⁻¹)	T_2^B (μs)	R_1 (s ⁻¹)	f (%)	k (s ⁻¹)
White matter											
Cerebral peduncle	0.933	14.81	2.064	11.560	1.088	16.54	2.353	11.556	0.928	14.73	2.097
Corona radiata	0.894	13.87	1.979	11.731	1.032	15.44	2.247	11.722	0.889	13.87	2.019
Corpus callosum, genu	0.966	15.36	2.702	9.844	1.133	17.28	3.115	9.836	0.959	15.30	2.758
Corpus callosum, splenium	0.942	14.92	2.517	10.197	1.105	16.75	2.890	10.187	0.940	14.90	2.570
Frontal white matter	0.898	13.93	2.161	11.231	1.036	15.49	2.445	11.223	0.892	13.90	2.196
Internal capsule, anterior limb	0.932	13.88	2.327	10.171	1.085	15.52	2.651	10.162	0.934	13.91	2.378
Internal capsule, posterior limb	0.903	15.33	2.048	11.836	1.057	17.20	2.356	11.829	0.896	15.26	2.092
Middle cerebellar peduncle	0.855	14.28	1.993	10.473	0.999	15.99	2.220	10.443	0.855	14.33	1.990
Occipital white matter	0.924	14.79	1.898	10.628	1.080	16.73	2.198	10.621	0.919	14.89	1.956
Gray matter											
Cerebral cortex	0.739	6.6	1.102	9.023	0.781	6.89	1.122	8.987	0.729	6.58	1.072
Caudate nucleus	0.655	6.42	1.321	9.628	0.702	6.71	1.380	9.619	0.657	6.43	1.322
Putamen	0.710	7.29	1.432	9.736	0.770	7.66	1.512	9.728	0.714	7.29	1.439
Substantia nigra	0.788	8.59	1.371	9.817	0.863	9.14	1.462	9.808	0.789	8.59	1.375
Thalamus	0.707	8.77	1.569	10.208	0.780	9.36	1.682	10.198	0.711	8.8	1.583

inconsistent for different tissues types in different pathological conditions. It is also important to emphasize that apparent R_1 values obtained from the standard single-compartment VFA technique are biased proportionally to f , and hence represent nonspecific measures containing contributions from both the intrinsic T_1 relaxation properties of water protons in tissues and the cross-relaxation between two proton pools.

We demonstrated that the accuracy of CRI estimates can be noticeably improved with the proposed combined data fit algorithm. Our mCRI data processing approach does not require any additional measurements, thus maintaining the same time-efficiency as the original CRI technique. The mCRI method yields unbiased VFA R_1 estimation, resulting in a decrease in R_1 values by approximately 15% in WM and 8% in GM (Tables 3 and 4), which agrees well with the bias predicted earlier (24). In addition to the mCRI fit, we have proposed a simple analytical first-order approximated correction formulas allowing recalculation of original CRI-based parameters. The residual bias of such correction was shown both theoretically and experimentally to increase with macromolecular content due to violation of the first-order approximation. It may reach about 2% for k and 1% for both f and R_1 in the ranges of physiologically reasonable values for brain tissues. Nevertheless, the first-order correction employed as a simple postprocessing step in the original CRI processing pipeline (Fig. 1) may be a valid alternative to mCRI when either faster processing is required or previously computed parameter values

need to be refined. As the residual error after first-order correction increases with f , care must be taken when applying this approach to tissues with a markedly high macromolecular content. Additionally, a combination of either mCRI fit or the first-order correction with the recent single-point CRI technique (12) provides a promising approach for the fast unbiased estimation of water proton R_1 values within the VFA method (35). Finally, it should be pointed out that other sources of bias in the VFA method need to be eliminated in conjunction with the proposed methodology, similar to the procedures described in this study. Practically, VFA R_1 mapping should be performed with a 3D sequence providing a uniform slab profile, B_1 correction, and appropriate spoiling conditions (30,31).

The described analysis and correction methods have several potential limitations. One is the fundamental limitation of the two-pool model for accurate description of multiple exchanging compartments in biological tissues (36,37). Another is a specific assumption about the longitudinal relaxation rate of the bound pool R_1^B . Particularly, a recent study (26) demonstrated that widely adapted approximations $R_1^B = 1 \text{ s}^{-1}$ (2,5) or $R_1^B = R_1^F$ (6,12) may considerably underestimate actual values of this parameter. Accordingly, this may cause an additional bias in the two-pool model parameters obtained using all qMT techniques based on the above assumptions about R_1^B . However, it remains unclear at this point whether a faster longitudinal relaxation rate of the bound pool protons is an intrinsic property of macromolecular protons or a manifestation of more complex equilibria involving water proton fractions with different mobilities. The later hypothesis is logical in view of a shorter T_1 found for the short- T_2 water fraction commonly termed “myelin water” (36,38–41). However, another limitation is the assumption about a negligible effect of the excitation pulse on the bound pool. This approximation is common for off-resonance pulsed quantitative MT methods employing low-angle excitation pulses (5–7,10,12), which causes negligible on-resonance saturation of the bound pool magnetization. However, as was shown earlier (25),

Table 4

Average Relative Bias Between mCRI and CRI Without and With First-Order Correction Calculated from In Vivo ROI Measurements (Table 3)

	CRI				First-order correction		
	R_1 (%)	f (%)	k (%)	T_2^B (%)	R_1 (%)	f (%)	k (%)
WM	15.33	11.34	13.21	0.09	-0.41	-0.06	1.85
GM	7.94	5.39	5.2	0.15	0.03	0.05	0.06

Bold font indicates significantly different results ($P < 0.05$).

the effect of on-resonance saturation should be taken into account for sequences with very short T_R and high flip angles, the conditions typical for the balanced steady state precession imaging. In the two-pool formalism with pulsed excitation (Eq. [1]), on-resonance saturation of the bound pool can be taken into account by assigning an actual saturation factor $S_b < 1$ in the diagonal matrix \mathbf{C} . Corresponding S_b values can be estimated from the properties of the excitation pulse (duration and flip angle) and a spectral line shape of the bound pool (11,22). Based on this approach, we found for a particular pulse used in our sequence that on-resonance saturation of the bound pool results in an almost negligible effect on the accuracy of the two-pool model parameters determined by mCRI ($<1\%$ relative error for comparison between fits with actual S_b vs. $S_b = 1$). However, this aspect of the technique could be important in the context of its standardization for future multicenter clinical studies since variations in the shape, duration, and flip angle of the excitation pulse may introduce a small but non-negligible bias dependent on a particular sequence implementation. Similarly, the approximation of the effect of the excitation pulse on the free pool by the term $\cos \alpha$ in the matrix \mathbf{C} (Eq. [1]) may not be absolutely correct due to relaxation during RF pulses of finite duration. Such an effect has been recently described (42), and its role for both VFA R_1 and CRI parameter measurements remains to be investigated. In summary, while this study relies on the commonly accepted in the quantitative MT methodology approximations, future refinements of CRI accuracy seem to be possible based on accommodation of multicompartment magnetization exchange schemes and a more rigorous analysis of magnetization dynamics during RF pulses.

CONCLUSIONS

This study demonstrates on the example of CRI that the accuracy of quantitative MT imaging can be considerably improved by taking into account the contribution of MT-induced biexponential longitudinal relaxation into VFA R_1 measurements. We have developed the two technical approaches allowing correction of biases in CRI parameter estimates caused by the MT-induced biexponential behavior of longitudinal relaxation of water spins based on either the global fit of both VFA and MT SPGR data to the two-pool signal model or the simple analytical recalculation formulas for key cross-relaxation parameters. Although the choice between these techniques depends on a tradeoff between the correction accuracy and image processing speed, both approaches do not require extra data compared to the original CRI method.

ACKNOWLEDGMENTS

The authors like to thank Dr. Richard Kijowski for valuable comments.

REFERENCES

- Wolff SD, Balaban RS. Magnetization transfer contrast (MTC) and tissue water proton relaxation in vivo. *Magn Reson Med* 1989;10:135–144.

- Henkelman RM, Huang X, Xiang QS, et al. Quantitative interpretation of magnetization transfer. *Magn Reson Med* 1993;29:759–766.
- Doussot V, Grossman RI, Ramer KN, et al. Experimental allergic encephalomyelitis and multiple sclerosis: lesion characterization with magnetization transfer imaging. *Radiology* 1992;182:483–491.
- Helms G, Dathe H, Kallenberg K, et al. High-resolution maps of magnetization transfer with inherent correction for RF inhomogeneity and T1 relaxation obtained from 3D FLASH MRI. *Magn Reson Med* 2008;60:1396–1407.
- Sled JG, Pike GB. Quantitative imaging of magnetization transfer exchange and relaxation properties in vivo using MRI. *Magn Reson Med* 2001;46:923–931.
- Yarnykh VL. Pulsed Z-spectroscopic imaging of cross-relaxation parameters in tissues for human MRI: theory and clinical applications. *Magn Reson Med* 2002;47:929–939.
- Ramani A, Dalton C, Miller DH, et al. Precise estimate of fundamental in-vivo MT parameters in human brain in clinically feasible times. *Magn Reson Imaging* 2002;20:721–731.
- Gochberg DF, Gore JC. Quantitative imaging of magnetization transfer using an inversion recovery sequence. *Magn Reson Med* 2003;49:501–505.
- Tozer D, Ramani A, Barker GJ, et al. Quantitative magnetization transfer mapping of bound protons in multiple sclerosis. *Magn Reson Med* 2003;50:83–91.
- Yarnykh VL, Yuan C. Cross-relaxation imaging reveals detailed anatomy of white matter fiber tracts in the human brain. *Neuroimage* 2004;23:409–424.
- Ropele S, Seifert T, Enzinger C, et al. Method for quantitative imaging of the macromolecular 1H fraction in tissues. *Magn Reson Med* 2003;49:864–871.
- Yarnykh VL. Fast macromolecular proton fraction mapping from a single off-resonance magnetization transfer measurement. *Magn Reson Med* 2012;68:166–178.
- Dortch RD, Li K, Gochberg DF, et al. Quantitative magnetization transfer imaging in human brain at 3 T via selective inversion recovery. *Magn Reson Med* 2011;66:1346–1352.
- Gloor M, Scheffler K, Bieri O. Quantitative magnetization transfer imaging using balanced SSFP. *Magn Reson Med* 2008;60:691–700.
- Soellinger M, Langkammer C, Seifert-Held T, et al. Fast bound pool fraction mapping using stimulated echoes. *Magn Reson Med* 2011;66:717–724.
- Underhill HR, Rostomily RC, Mikheev AM, et al. Fast bound pool fraction imaging of the in vivo rat brain: association with myelin content and validation in the C6 glioma model. *Neuroimage* 2011;54:2052–2065.
- Schmierer K, Tozer DJ, Scaravilli F, et al. Quantitative magnetization transfer imaging in postmortem multiple sclerosis brain. *J Magn Reson Imaging* 2007;26:41–51.
- Ou X, Sun SW, Liang HF, Song SK, Gochberg DF. Quantitative magnetization transfer measured pool-size ratio reflects optic nerve myelin content in ex vivo mice. *Magn Reson Med* 2009;61:364–371.
- Dula AN, Gochberg DF, Valentine HL, et al. Multiexponential T2, magnetization transfer, and quantitative histology in white matter tracts of rat spinal cord. *Magn Reson Med* 2010;63:902–909.
- Samsonov A, Alexander AL, Mossahebi P, et al. Quantitative MR imaging of two-pool magnetization transfer model parameters in myelin mutant shaking pup. *Neuroimage* 2012;62:1390–1398.
- Wang HZ, Riederer SJ, Lee JN. Optimizing the precision in T1 relaxation estimation using limited flip angles. *Magn Reson Med* 1987;5:399–416.
- Edzes HT, Samulski ET. Cross relaxation and spin diffusion in the proton NMR of hydrated collagen. *Nature* 1977;265:521–523.
- Prantner AM, Bretthorst GL, Neil JJ, et al. Magnetization transfer induced biexponential longitudinal relaxation. *Magn Reson Med* 2008;60:555–563.
- Ou X, Gochberg DF. MT effects and T1 quantification in single-slice spoiled gradient echo imaging. *Magn Reson Med* 2008;59:835–845.
- Bieri O, Scheffler K. On the origin of apparent low tissue signals in balanced SSFP. *Magn Reson Med* 2006;56:1067–1074.
- Helms G, Hagberg GE. In vivo quantification of the bound pool T1 in human white matter using the binary spin-bath model of progressive magnetization transfer saturation. *Phys Med Biol* 2009;54:N529–N540.
- Ernst RR, Anderson WA. Application of Fourier transform spectroscopy to magnetic resonance. *Rev Sci Instrum* 1966;37:93–102.
- Portnoy S, Stanisz GJ. Modeling pulsed magnetization transfer. *Magn Reson Med* 2007;58:144–155.

29. Morrison C, Henkelman RM. A model for magnetization transfer in tissues. *Magn Reson Med* 1995;33:475–482.
30. Koenig SH, Brown RD 3rd, Ugolini R. Magnetization transfer in cross-linked bovine serum albumin solutions at 200 MHz: a model for tissue. *Magn Reson Med* 1993;29:311–316.
31. Yarnykh VL. Optimal radiofrequency and gradient spoiling for improved accuracy of T1 and B1 measurements using fast steady-state techniques. *Magn Reson Med* 2010;63:1610–1626.
32. Yarnykh VL. Actual flip-angle imaging in the pulsed steady state: a method for rapid three-dimensional mapping of the transmitted radiofrequency field. *Magn Reson Med* 2007;57:192–200.
33. Reeder SB, Pineda AR, Wen Z, et al. Iterative decomposition of water and fat with echo asymmetry and least-squares estimation (IDEAL): application with fast spin-echo imaging. *Magn Reson Med* 2005;54:636–644.
34. Underhill HR, Yuan C, Yarnykh VL. Direct quantitative comparison between cross-relaxation imaging and diffusion tensor imaging of the human brain at 3.0 T. *Neuroimage* 2009;47:1568–1578.
35. Mossahebi P, Samsonov AA. Rapid and accurate variable flip angle T1 mapping with correction of on-resonance MT effects. In Proceedings of the 20th Annual Meeting of ISMRM, Melbourne, Australia, 2012. Abstract 4267.
36. Stanisz GJ, Kecojovic A, Bronskill MJ, et al. Characterizing white matter with magnetization transfer and T(2). *Magn Reson Med* 1999;42:1128–1136.
37. Levesque IR, Pike GB. Characterizing healthy and diseased white matter using quantitative magnetization transfer and multicomponent T(2) relaxometry: a unified view via a four-pool model. *Magn Reson Med* 2009;62:1487–1496.
38. Does MD, Gore JC. Compartmental study of T(1) and T(2) in rat brain and trigeminal nerve in vivo. *Magn Reson Med* 2002;47:274–283.
39. Koenig SH, Brown RD 3rd, Spiller M, et al. Relaxometry of brain: why white matter appears bright in MRI. *Magn Reson Med* 1990;14:482–495.
40. MacKay A, Whittall K, Adler J, et al. In vivo visualization of myelin water in brain by magnetic resonance. *Magn Reson Med* 1994;31:673–677.
41. Deoni SC, Rutt BK, Arun T, et al. Gleaning multicomponent T1 and T2 information from steady-state imaging data. *Magn Reson Med* 2008;60:1372–1387.
42. Boulant N. T1 and T2 effects during radio-frequency pulses in spoiled gradient echo sequences. *J Magn Reson* 2009;197:213–218.

Simultaneous Mapping of B1 and Flip Angle by Combined Bloch-Siebert, Actual Flip-angle Imaging (BS-AFI)

Samuel A. Hurley¹, Pouria Mossahebi^{2,3}, Kevin M. Johnson¹, and Alexey A. Samsonov³

¹Medical Physics, University of Wisconsin, Madison, WI, United States, ²Biomedical Engineering, University of Wisconsin, Madison, WI, United States, ³Radiology, University of Wisconsin, Madison, WI, United States

Introduction: The accuracy of many quantitative MRI (qMRI) methods depends critically on accurate knowledge of radiofrequency transmit field amplitude (B_1) or flip angle (FA). While the terms B_1 and FA are sometimes used interchangeably, FA depends not only on B_1 but also additional factors such as RF pulse envelope, slab profile, tissue relaxation parameters, and B_0 effects that can lead to substantial errors when correcting qMRI methods [1]. In general, B_1 correction is most appropriate for nonselective pulses (e.g. off-resonance pulse in magnetization transfer (MT) or a hard 180° pulse in inversion recovery) while FA correction is appropriate for selective excitation pulses (e.g. variable flip angle T_1 mapping). Many methods such as quantitative MT [2,3] and Look-Locker T_1 mapping utilize both types of pulses in the same experiment, however to date no consideration has been made of separate B_1 and FA effects. Therefore, the measurement and correction of both parameters may increase the overall accuracy of such methods.

Bloch-Siebert B_1 mapping (BS) is a recently proposed phase-based method to rapidly map B_1 with an off-resonant nonselective pulse [4], while Actual Flip-angle Imaging (AFI) is a method to map FA using the ratio of signals from two interleaved steady-state TRs [5]. We propose a novel combination of these two sequences, BS-AFI, to map FA using image magnitude and encode B_1 into the image phase with zero time penalty over AFI. Improved MT accuracy is demonstrated in phantom validations.

Methods: The BS-AFI pulse sequence was implemented on a GE MR750 (fig. 1). A standard AFI pulse sequence was implemented by the addition of a second $TR_2 (=5*TR_1)$ to an SPGR sequence; BS mapping was then added through the introduction of an 8ms Fermi-shaped off-resonance pulse just after the excitation pulse and just before phase encoding. As BS requires the phase differences of two $\pm\omega$ off-resonance pulses, a pulse at +4kHz is played during TR_1 and -4kHz during TR_2 . Four additional alternating pulses are played during TR_2 to maintain a pulsed steady-state saturation. A potential issue of this implementation is if MT saturation effects are different between TR_1 and TR_2 due to variation in center frequency with B_0 . However, since the TR of the AFI sequence is shorter than the timescale of MT exchange, we hypothesize that these alternating pulses will create an averaging effect and generate the same MT contrast in both images, eliminating any confounds to AFI quantification. The B_1 -dependant phase precession may also interfere with RF spoiling, however it was shown that the use of large spoiler gradients eliminates sensitivity to RF spoiling effects [6].

A cylindrical gelatin phantom was scanned at $64 \times 48 \times 52$ matrix and 1.5^3 mm^3 isotropic resolution in the coronal plane, then re-formatted to axial to visualize slab profile (vertical direction). BS-AFI and standard AFI scans were acquired with $TR_1/TR_2 = 36/180\text{ms}$ and $\alpha = 55^\circ$. Spoiled gradient echo (SPGR) scans were acquired with $TR = 36\text{ms}$ and $\alpha = [5 \ 10 \ 20 \ 30 \ 40]^\circ$. Ten MT-weighted SPGR were acquired with $TR = 36\text{ms}$, $\alpha = 10^\circ$, and offset frequency $\Delta = [1 \ 2.5 \ 4 \ 9 \ 13] \text{ kHz}$ for MT flip angles 500° and 920° . The SPGR and MT data were then fitted to a five-parameter model of MT (bound pool fraction, exchange rate, T_2 of bound pools, PD , and T_1 of free pool) [7]. The qMT data were corrected in three ways: using only the FA map to correct both excitation and MT pulse flip angles (FA only), using only the B_1 map to correct both (B_1 only), and using the BS-AFI FA to correct the excitation flip angle and B_1 to correct MT flip angle. B_0 correction was done using IDEAL [8].

Results: Mean error for the BS-AFI method, compared to separate AFI and Bloch-Siebert mapping, was $3.0 \pm 2.2\%$ in B_1 and $2.0 \pm 1.1\%$ in FA (fig. 2). Spatially varying differences between techniques were not observed, even in the presence of B_0 inhomogeneity (0–200 Hz within slice, as measured with IDEAL). SNR of the B_1 map was also improved (variance $\sigma_{\text{STANDARD}} = 0.0048 \text{ G}$, $\sigma_{\text{BS-AFI}} = 0.0037 \text{ G}$; small ROI in center of image) due to increased signal from a longer AFI TR_2 . qMT parameter maps using only FA or B_1 show distinct errors due to slab profile (fig. 3, see caption). BS-AFI maps show uniform measures along the slab direction (fig. 4).

Discussion & Conclusions: Simultaneous knowledge of B_1 and FA may be useful for a wide range of qMRI applications that employ both selective and non-selective RF pulses, including quantitative MTI, Look-Locker T_1 mapping, and the correction of stimulated echoes in a multi-exponential T_2 CPMG experiment [9]. Although errors in FA due to slab profile can be minimized in other ways, such as the use of a longer optimized RF pulse or nonselective 3D imaging, such approaches are not always feasible. Nonselective imaging is only acceptable in applications where the object is sufficiently small to be covered by two phase encoding directions in a reasonable scan time, and may lead to additional errors due to increased sensitivity to B_0 variations. Pulses that are optimized for slab selection may still have residual errors in a significant number of slices, as we have observed errors greater than 5% in quantitative maps occur in 1/3 of our slices. These approaches also do not consider variations in FA due to B_0 or the relaxation properties of tissue (e.g. T_2 relaxation in ultrashort TE sequences).

In contrast, the BS-AFI method enables rapid and accurate qMRI with sequences employing any combination of selective or non-selective RF pulse types. The key feature of the pulse sequence is encoding the two alternating off-resonance shifts into two AFI TRs. This may potentially influence contrast of AFI images differently if TR is long, however no variations were observed in our experiment using typical AFI parameters. [3,6]. This averaging effect may be beneficial not only in the context of BS-AFI, but also B_0 -insensitive qMT or MT ratio measurements, and will be the subject of future work. In conclusion, we present a method to simultaneously map B_1 and FA that is robust to B_0 and MT errors and incurs no scan time penalty over the traditional AFI method. In context of MT, separate measurement of FA for excitation flip angle correction and B_1 for MT power correction led to a significant increase in the accuracy of bound pool fraction. In addition to elongated scan times, separate acquisition of such maps may result in reduced consistency of B_1 and FA mapping due to patient motion.

References: [1] Wang et al. MRM 2006;56:463 [2] Sled JG et al. MRM 2001;46:923 [3] Yarnykh VL MRM 2002;47:929 [4] Sacolick, LI et al. MRM 2010;63:1315 [5] Yarnykh VL MRM 2007;57:192. [6] Yarnykh VL MRM, 2010;63:1610 [7] Mossahebi P et al. WMSG 2011 p13. [8] Yu, H. JMRI 2007;26:1153 [9] Prasloski T. et al. MRM 2011 (in press). **Acknowledgements:** We acknowledge the financial support of the NIH (NINDS R01NS065034).

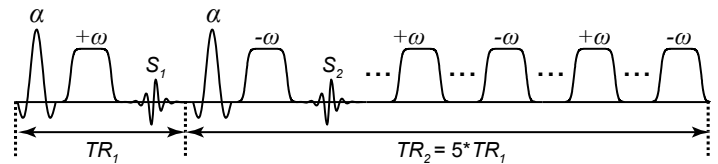


Fig 1: Diagram of BS-AFI pulse sequence. α is a slab-selective excitation pulse, while $\pm\omega$ is a nonselective Fermi pulse applied at $\pm\omega$ Hz with respect to center frequency. Additional Fermi pulses continue to play at regular intervals during the second TR (figure compressed to save space).

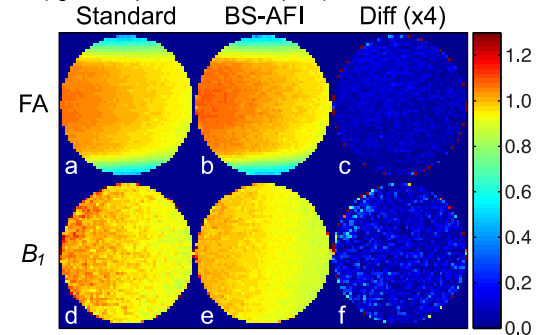


Fig 2: Comparison of standard AFI (a) & BS (d) methods to the combined BS-AFI approach (b,e), normalized by nominal flip angle. Significant differences between FA (a,b) and B_1 (d,e) are observed, primarily due to slab profile (vertical direction). Absolute error (c,f) is quite uniform, despite large off-resonance within slice (~200 Hz, not shown).

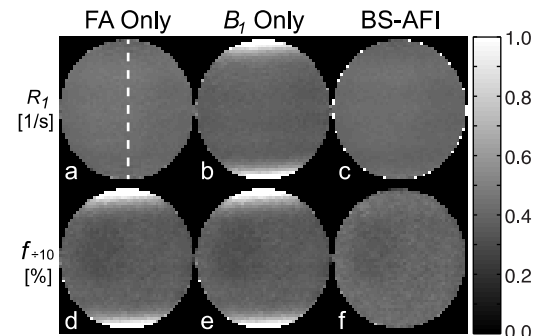


Fig 3: $R_1 (=1/T_1)$ (a-c) and bound pool fraction f (d-f) maps using three correction approaches. Note that R_1 mapping using B_1 correction (b) or correction of MT pulse with FA (d) both result in large residual errors due to slab profile. Similar errors were observed in PD and exchange rate (not shown).

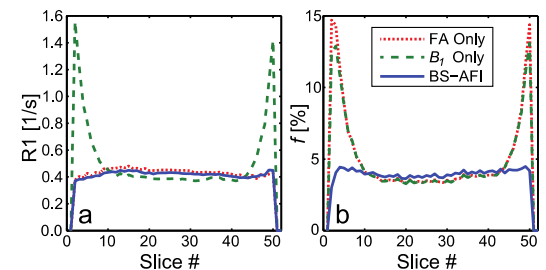


Fig 4: Plot of R_1 and f along slab profile (dash line in fig. 3a).

Improved Accuracy of Cross-Relaxation Imaging Using On-Resonance MT Effect Correction

Pouria Mossahebi¹, Vasily L. Yarnykh², and Alexey A. Samsonov³

¹Biomedical Engineering, University of Wisconsin, Madison, WI, United States, ²Radiology, University of Washington, Seattle, WA, United States, ³Radiology, University of Wisconsin, Madison, WI, United States

INTRODUCTION: Over past years, several methods have been proposed for quantitative mapping of molecular parameters describing the magnetization transfer (MT) effect within the two-pool model (bound pool fraction f , cross-relaxation rate k , and transverse relaxation times of the bound pool T_2^B and free pool T_2^F) from a series of images with variable off-resonance saturation [1-4]. Resulting parametric maps are expected to provide new biomarkers in various neurological conditions. Particularly encouraging results were reported for the bound pool fraction, which provides strong associations with myelin content in neural tissues [5,6]. The common feature of the above methods is the need for complementary T_1 mapping, which allows decoupling of the two-pool model parameters from the longitudinal relaxation rate $R_1=1/T_1$. One of such methods, cross-relaxation imaging (CRI) [4] allows 3D acquisition with excellent speed and resolution based on combination of a limited number of MT-weighted images and variable flip angle (VFA) T_1 maps obtained using a fast spoiled gradient-echo (SPGR) sequence. However, recent studies showed that the on-resonance MT effect may cause a significant bias in the steady-state MR signal [7,8], if the model does not account for bi-exponential behavior of longitudinal relaxation occurring due to MT. This bias unavoidably introduces errors in VFA R_1 measurements [8], which may propagate into the two-pool model parameters measured by CRI. In this study, we theoretically and experimentally characterize systematic errors in CRI caused by MT-related bias in VFA R_1 mapping and propose a modified processing algorithm, which corrects for such errors and yields accurate quantitative MT parametric maps.

THEORY: In the standard CRI approach, reconstruction of parametric maps is performed in two steps [4]. During the first step, R_1 and proton density (PD) maps are calculated from VFA data by fitting the Ernst equation. This approach ignores coupling between R_1 and the rest of two-pool model parameters. During the second step, the matrix model of pulsed MT [4] is fitted to MT-weighted data, while R_1 is supplied as an external parameter. Prior to fit, MT data are normalized to the signal intensity obtained without saturation to exclude PD. Depending on the sampling scheme and constraints imposed on certain two-pool model parameters, either all four parameters (f , k , T_2^B , T_2^F) or their subsets can be fitted [4,5,9]. As an alternative to this approach, we modified the CRI model to simultaneously perform global fit of VFA and MT data, which yields all parameters (PD , R_1 , f , k , T_2^B , T_2^F) with full consideration of coupling between them. Theoretically, MR-related errors in R_1 measured by the VFA method can be caused by the two mechanisms unaccounted within the standard single-pool signal model. These are on-resonance saturation of the bound pool by the excitation pulse and bi-exponential relaxation during TR, where a contribution of the fast-relaxing component becomes more significant at short TR. To estimate relative roles of these factors, the model was further modified to include an additional term to account for the effect of excitation pulse on semisolid pool [7] calculated by Bloch equation simulations.

METHODS: Volunteer data were obtained on a 3.0T GE MR750 (Waukesha, WI) scanner. To correct for B1 and B0 inhomogeneity, flip angle (B1) and field (B0) maps were measured by optimized AFI method [10] and IDEAL [11], respectively. 3D VFA data were acquired with FAs $\alpha=[5,10,20,30]^\circ$. Ten MT SPGR datasets were acquired ($\alpha=10^\circ$, $\Delta=0.8, 2.5, 5.9, 13$ kHz, $\alpha_{MT}=[500,1100]^\circ$, 18ms Fermi pulse). Additional dataset without saturation was acquired at offset frequency 200kHz to normalize MT data for the original CRI approach. All data were acquired with TR/TE=40/2.0ms, 240×180×80mm FOV, 128×96×40 matrix. The standard CRI processing workflow was implemented according to [4,9]. In modified CRI, all parametric maps were generated by fitting the SPGR and MT data simultaneously to the general signal equation based on the two-pool matrix steady-state MT model [2,4] using in-house-written C and MATLAB (MathWorks, Natick, MA) software utilizing a trust-region-reflective algorithm for nonlinear least squares fitting of each voxel.

RESULTS: Synthetic MT and SPGR data for white matter (WM) and gray matter (GM) ROIs were generated based on the parameters given in [9]. Table 1 shows that on-resonance MT effect introduces significant bias to all quantitative MT parameters except T_2^B when estimated with original CRI method. The dominant cause of errors was found to originate from effective shortening of T_1 in the two-pool system due to bi-exponential relaxation, whereas saturation of the bound pool by the excitation pulse produced an almost negligible effect (~1%). Qualitative (Table 2) and quantitative in vivo comparisons (Fig. 1) of original and modified CRI methods are consistent with simulations and demonstrate compatible effect sizes in all parameters.

DISCUSSION: We showed that errors caused by unaccounted effect of MT on VFA R_1 measurements result in significant bias in estimates of CRI parameters. Generally, this bias depends on the values of the two-pool model parameters, which makes it inconsistent for different tissues types and in different pathological conditions. Approximately, this type of errors can be characterized as overestimation of R_1 , f , and k , and underestimation of T_2^F with a relative effect size on the order of $f\%$. Our results show that accuracy of the original CRI approach is noticeably improved with the proposed combined data fit to the modified CRI model, which accounts for MT effects on the apparent R_1 . In brain imaging, the method also corrected VFA R_1 values by approximately 15% in WM and 6% in GM, which agrees well with the bias predicted by [8]. Finally, the modified CRI fit does not require acquisition of normalizing

CONCLUSIONS: This study demonstrates that separate treatment of VFA and MT data in the CRI method causes non-negligible systematic errors in both R_1 and cross-relaxation parameters. Our modified CRI data processing approach effectively corrects these errors and does not require any additional measurements, thus maintaining time-efficiency of the original CRI technique.

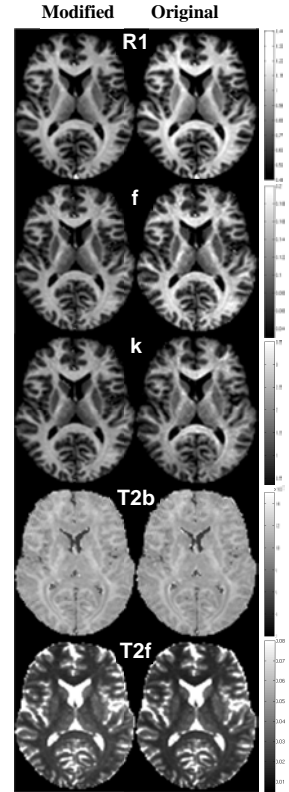


Figure 1. Parametric MT maps estimated using modified (left) and original (right) CRI.

	R_1	f	k	T_2^b	T_2^f
WM (Corpus Callosum)	15.27%	11.24%	13.97%	2.76e-4%	-11.49%
GM (Putamen)	8.16%	5.65%	6.49%	2.63e-4%	-5.64%

Table 1. Errors in two-pool MT model parameters in original CRI fit due to unaccounted on-resonance MT effects (simulations).

	Modified CRI					Original CRI				
	$R_1 (s^{-1})$	$f (\%)$	$k (s^{-1})$	$T_2^b (\mu s)$	$T_2^f (ms)$	$R_1 (s^{-1})$	$f (\%)$	$k (s^{-1})$	$T_2^b (\mu s)$	$T_2^f (ms)$
WM (Corpus Callosum)	0.977±0.032	14.00±0.46	2.635±0.218	10.31±0.32	25.06±2.23	1.104±0.038	16.62±0.78	2.815±0.242	10.15±0.32	21.77±1.95
GM (Putamen)	0.726±0.039	7.21±0.39	1.359±0.094	10.40±0.31	33.06±2.89	0.774±0.044	8.12±0.49	1.363±0.098	10.24±0.30	30.95±2.70

Table 2. In vivo measurements of CRI parameters using modified and original CRI.

REFERENCES: [1] Sled JG. et al. MRM 2001; 46. [2] Yarnykh VL. MRM 2002; 47:929. [3] Tozer D. et al. MRM 2003; 50. [4] Yarnykh VL. et al. Neuroimage 2004; 23:409. [5] Underhill HR. et al. NeuroImage 2011; 54:2052. [6] Samsonov A et al. ISMRM 2010, 4876. [7] Bieri O. et al. MRM 2006; 56:1067. [8] Ou X. et al. MRM 2008; 59:835. [9] Underhill HR. et al. NeuroImage 2009; 47:1568. [10] Yarnykh VL. MRM 2007; 57:192. [11] Reeder SB. et al. MRM 2005; 52.

ACKNOWLEDGEMENTS: This work was supported by NIH (R01NS065034).

Optimization Strategies for Accurate Quantitative MT Imaging

Pouria Mossahebi¹, and Alexey A. Samsonov²

¹Biomedical Engineering, University of Wisconsin, Madison, WI, United States, ²Radiology, University of Wisconsin, Madison, WI, United States

INTRODUCTION: Quantification of two-pool MT (qMT) model parameters (longitudinal relaxation rate $R1$, bound pool fraction f , cross relaxation rate k , transverse relaxation times of the bound pool T_2^B , and free pool T_2^F) allows inferring useful information about MRI-invisible macromolecular tissue content such as myelin [1,2]. Many qMT methods such as cross-relaxation imaging (CRI) [3] use efficient pulsed MT in steady state, however data acquisition time may be too long for clinical applications. One CRI acceleration approach is to exclude T_2^F from estimation by sampling high offset frequencies ($\Delta > 2.5$ kHz) where direct saturation of free water is minimized. Going from 1.5T, the system used in early qMT applications [1-3], to 3T may improve CRI by utilizing the field-dependent SNR increase [4]. However, translation to 3T faces an increased specific absorption rate (SAR); the related decrease in highest attainable MT flip angle may lead to SNR loss in parametric maps. This work studies challenges of CRI at 3T and proposes several optimizations at both 1.5 and 3T field strengths.

METHODS AND RESULTS: Effect of Experiment Design: Two families of experiment designs were studied: 1) Standard CRI with higher $\Delta = 2.5, 5, 9, 13$ kHz (only $R1, f, k, T_2^B$ are estimated). 2) Extended design with additional optimized low $\Delta = 0.8$ kHz (T_2^F is also estimated). Data were synthesized for white matter for 18ms Fermi MT pulse with flip angles 500° (1.5T and 3T) and 1100° (3T) / 1600° (1.5T) (maximal allowed values on our GE Signa 1.5T and MR750 3T for the given patient weight and coil type). Monte-Carlo simulations were performed to find noise level σ in qMT estimates (Fig. 1). Efficiency was defined as $1/\sigma$ and did not include field dependent SNR gain. Using low Δ significantly improved estimation of CRI measures (especially k) despite dimensionality increase (T_2^F estimation). Effect of MT Pulse Shape: The effect of using MT pulses with low (Gaussian) and high (Fermi) SAR-efficiency [6] on the qMT mapping performance were examined for Design #2. The pulses had same duration and peak SAR. Fermi pulse was more SNR-efficient for parameter estimation than Gaussian pulse with most gain observed for k (Table 1). Effect of MT Pulse Bandwidth: Higher BW (shorter) Fermi pulse may cause large errors in qMT maps using low offset frequencies (Table 2). The standard approach is to use Lorentzian lineshape to model the effect of MT pulse on free pool. The approach fails to adequately describe the behavior of free pool in the range < 1 kHz (Fig. 2c). The deviation is due to Rabi oscillations arising in near-resonance excitation regime, the effect highly dependent on local B1 distribution (Fig. 2a) not accounted for in realistic qMT models [5]. The MT signal is much more sensitive to changes in B0 and B1 for shorter pulse (Figs. 2a,b). The effect is hard to account for in realistic qMT models [5] because it is highly dependent on local distribution of transmit field B1 (Fig. 2). The accuracy loss for 20 ms pulse (narrower BW) was much less for most measures ($R1, f, k, T_2^B$) while still significant for T_2^F (Table 2). Phantom Results: MT weighted data of FBRIN phantom [7] were acquired at offset frequencies 0.6 and 20kHz with 8ms Fermi MT pulse with flip angle 750° . Range of offset frequency in the phantom was provided using shim gradients and measured using IDEAL [8]. Flip angle map was measured by optimized AFI method [9]. The 3D images of MT ratio (SMT(0.6kHz)/SMT(20kHz)) were plotted against local flip angle ($\sim B1$) and B0 values (Fig. 2d). The observed oscillations were consistent with simulations for free water magnetization (Fig. 2b) (full quantitative comparison between theoretical predication phantom data was not made because of additional MT effect in the agar phantom and uncertainties in B1 field determination from actual flip angle values).

DISCUSSION: We studied several ways to optimize efficiency of CRI at both 1.5 and 3T. We showed (for 3T case) that the CRI efficiency may be improved by including extra sample(s) from low Δ range (< 1 kHz). Further, we demonstrated that SAR-efficient pulses may provide additional large efficiency gains in CRI. At the same time, high BW SAR-efficient pulses may lead to a significant error in qMT measures for the low offset frequency designs. One simple solution is to resort to longer SAR-efficient pulses. We found the reasonable tradeoff to be 16-20 ms Fermi pulses. We are currently working on MT pulse BW correction for more efficient imaging with shorter pulses. We conclude that CRI and other related qMTI methods may be optimized as proposed here to significantly improve their accuracy and efficiency.

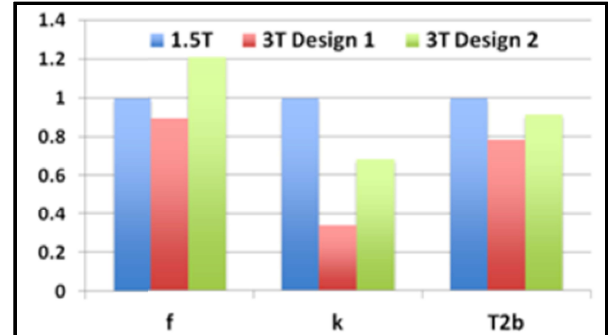


Fig. 1: Relative efficiency of CRI parameter mapping at 3T using regular (#1) and extended (#2) designs (normalized to 1.5T values).

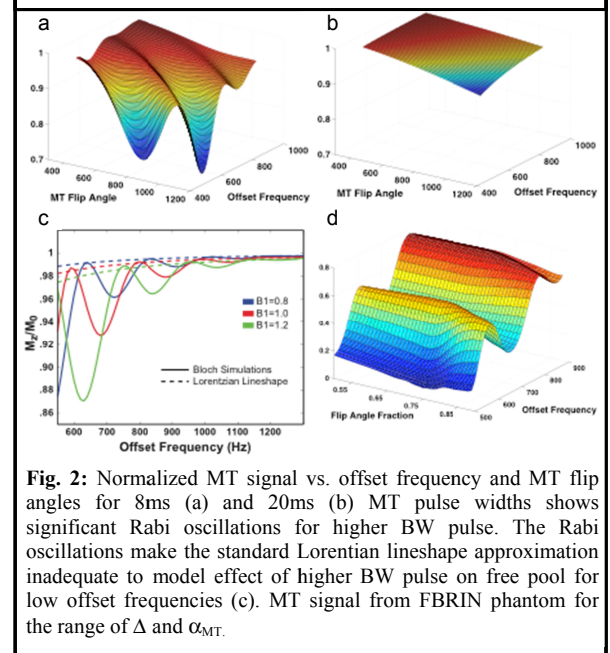


Fig. 2: Normalized MT signal vs. offset frequency and MT flip angles for 8ms (a) and 20ms (b) MT pulse widths shows significant Rabi oscillations for higher BW pulse. The Rabi oscillations make the standard Lorentzian lineshape approximation inadequate to model effect of higher BW pulse on free pool for low offset frequencies (c). MT signal from FBRIN phantom for the range of Δ and α_{MT} .

$R1$	f	k	T_2^B	T_2^F
1.0413	1.5820	2.9149	1.7558	1.9361

Table 1: Efficiency of Fermi relative to that of Gaussian MT pulses ($\sigma_{\text{gauss}}/\sigma_{\text{fermi}}$).

	$R1$	f	k	T_2^B
8ms Fermi	-11.33	40.7	-48.7	18.23
20ms Fermi	-0.01	-0.12	-3.24	-0.32

Table 2: Percent of error in CRI parameters for different MT pulse widths (Design #2).

REFERENCES: [1] Sled JG. et al. MRM 2001; 46. [2] Tozer D. et al. MRM 2003; 50. [3] Yarnykh VL. et al. NeuroImage 2004; 23. [4] Yarnykh VL. et al. NeuroImage 2009; 47. [5] Portnoy S. et al. MRM 2007; 58. [6] Bernstein MA, et al. Handbook of MRI Pulse Sequences, 2004. [7] <http://www.birmcommunity.org>. [8] Reeder SB. et al. MRM 2005; 52. [9] Yarnykh VL. MRM 2007; 57.

ACKNOWLEDGEMENTS:
The work was supported by NIH grant R01NS065034

High Resolution, Motion Corrected Mapping of Macromolecular Proton Fraction (MPF) In Clinically Acceptable Time Using 3D Undersampled Radials

Alexey Samsonov¹, Pouria Mossahebi², Ashley Anderson³, Julia Velikina⁴, Kevin M. Johnson⁵, Sterling C Johnson⁵, John O Fleming⁶, and Aaron Field⁷

¹Radiology, University of Wisconsin, Madison, United States, ²Biomedical Engineering, University of Wisconsin, Madison, United States, ³Medical Physics, University of Wisconsin, Madison, WI, United States, ⁴Medical Physics, University of Wisconsin, Madison, Wisconsin, United States, ⁵Medicine, University of Wisconsin, Madison, Wisconsin, United States, ⁶Neurology, University of Wisconsin, Madison, Wisconsin, United States, ⁷Radiology, University of Wisconsin, Madison, Wisconsin, United States

Introduction: Two-pool modeling of magnetization transfer (MT) effects yields a unique set of measures sensitive to different tissue composition properties [1-4]. The key parameter of interest in this model is a macromolecular pool fraction (MPF), a potential biomarker of myelin in neural tissues [5-7]. Particularly promising findings were recently reported on the utility of MT-based measures including MPF for assessment of white and gray matter (WM/GM) myelin status in multiple sclerosis (MS) [7-8]. In particular, MPF in GM was found to be the strongest independent predictor of disability in MS patients [7,9]. Given that cortical demyelination has been recognized as an important pathological substrate in MS [10,11], the availability of such a myelin biomarker may greatly facilitate our understanding of GM involvement in MS disease course. However, traditional MPF mapping within clinical scan time is a relatively low-resolution methodology not fully compatible with current standards for imaging of cortical structures (~1 mm isotropic) or achieving higher fidelity in detection of demyelinating lesions in WM. Longer scan times needed to attain the resolution makes MPF mapping susceptible to small patient motion. The purpose of this work was to develop a clinically feasible, high resolution, motion corrected MPF mapping protocol compatible with clinical standards for GM assessment.

Methods: Three Point MPF Mapping: Fast cross-relaxation imaging (CRI) [13] was proposed as an efficient strategy for MPF mapping with reduced number of acquisition points including spoiled gradient echo (SPGR) with (MT_{ON}) and without (MT_{OFF}) MT weightings, and two variable flip angle (VFA) SPGR datasets for pre-requisite R_1 mapping. This method imposes realistic constraints onto the subset of two-pool MT model parameters (exchange rate R and T_2 of bound protons) and prescribes an optimized experimental design to provide least sensitivity to these constrained quantities. We combined the constrained approach with a modified CRI (mCRI) fit [13] to remove the bias in estimation due to on-resonance MT effects and also further reduce the number of measurements by 25% (from four to three). Our approach (3p-mCRI) performs simultaneous fitting of two VFA and one MT SPGR datasets to the unified signal model, which allowed estimation of MPF, R_1 , and proton density terms without the MT_{OFF} dataset [14]. 3D Undersampled Motion-Corrected Radial Acquisition: To study feasibility of high resolution, motion-corrected MPF mapping in clinically feasible time, the method was implemented with 3D radial undersampled acquisition trajectory. 3D radial sampling trajectory provides mild undersampling artifacts allowing accelerated imaging without noise-amplifying matrix-inverse-based parallel MRI techniques (pMRI). Additionally, a notable advantage of radials is the ability to implement interleaved projection ordering to acquire low-resolution motion-tracking navigators from the oversampled k -space center. We implemented 2D bit reversed scheduling of projections to acquire such navigators to enable retrospective motion correction as described in [15]. As non-uniform k -space sampling density of 3D radials incurs additional scan time penalty (a factor of ~1.57), we designed variable density readout (VDS) to partially compensate for this efficiency loss, which theoretically allows improving SNR efficiency by ~1.37 compared to uniform readout trajectory of equivalent length [16]. Data Acquisition: Cartesian Protocols: SPGR: TR=23ms, α =[4,24]°; MT SPGR: TR=37ms, α =12°, Δ =4 kHz, α_{MT} =[850]°, 18ms Fermi pulse; Common parameters: TE=3.7 ms, 2x GRAPPA, 8 channel coil. 3D Radials: SPGR: TR=18ms, α =[4,22]°; MT SPGR: TR=33ms, α =13°, Δ =4 kHz, α_{MT} =[750]°, 12ms Fermi pulse; Common parameters: 22,000 projections (undersampling factor R=3.45), FOV=220, TE=6.2 ms, 32 channel coil. All protocols included AFI flip angle mapping [17]. Total scan time was: 15.5/29 min (Cartesian scans with 1.25/1 mm isotropic resolution, respectively), and 28 min for radial scans. Data were acquired using on a 3.0T GE MR750 (Waukesha, WI). Processing was done by in-house-written software [18]. Cortical thickness mapping was performed with FreeSurfer software [19].

Results: One healthy volunteer and one relapsing-remitting (RR) MS patient were scanned with the developed protocols. 3p-mCRI MPF mapping was first validated in Cartesian scans. Figure 1 compares cortical thickness measured with different imaging techniques. 3p-mCRI MPF outperforms the standard IR-SPGR sequence used most often for measurements of cortical atrophy. Figure 2 shows improved visualization of deep GM structures with MPF compared to IR-SPGR and R_1 maps (all 1 mm isotropic). The longitudinal stability of 3p-mCRI was tested in a RR MS patient during multiple visits. Figure 3 demonstrates excellent longitudinal consistency of 3p-mCRI MPF mapping. Figure 4a shows performance of 3D radial implementation of 3p-MRI MPF mapping. The protocol provides excellent depiction of cortical and deep GM structures. Figure 4b illustrates its motion correction capabilities of the radial protocol.

Discussion: We presented a series of methodological and technical developments aimed towards robust methodology for high resolution MPF mapping. Compared to early published protocols for fast MPF mapping [13,14], our 3D radial approach decreases voxel size by a factor of ~7-11 at the expense of ~2.2-2.5 times scan time increase, while maintaining adequate SNR (Fig. 4) and clinically acceptable scan time (<30 min). The imaging protocol derives from several sources, including minimalistic 3-point constrained mCRI approach, SNR-optimized 3D radials, and acquisition scheduling for motion correction. Acquisition of undersampled radials with 32-channel array did not require specialized pMRI reconstruction (well known property of radial sampling at low accelerations) and hence avoided noise amplifications common in matrix-inversion based pMRI techniques. However, the dedicated pMRI reconstruction may be required when imaging is performed with fewer coil elements, or when higher acceleration factors are targeted. The protocol provides motion-corrected and longitudinally stable MPF (and R_1) maps, which may establish it as a tool for high precision morphometric applications and GM/WM segmentation in longitudinal and cross-sectional studies (Figs. 1,3). Myelin-specific contrast obtained with MPF may be especially important to study diffuse changes in both GM and WM. Reduced partial voluming with CSF due to higher resolution may be important to provide imaging assessment of subpial GM involvement in MS, while stronger WM/GM contrast in MPF may help with detection/classification of demyelinating lesions at GM/WM junction.

REFERENCES: [1] Henkelmann et al. MRM1993; [2] Sled JG. et al. MRM2001; 46:923. [3] Yarnykh VL. MRM2002; 47:929. [4] Tozer D. et al. MRM2003; 50:83. [5] Underhill HR. et al. NeuroImage2011; 54:2052. [6] Samsonov A et al. Neuroimage2012; 62:1390. [7] Yarnykh VL. et al. ISMRM2013; 45. [8] Fisniku LK, Mult Scler. 2009;15(6):668-77. [9] Yarnykh VL. et al. ISMRM2013; 3613. [10] Kutzelnigg A. et al. Brain 2005; 128:2705. [11] Kidd T. et al. Brain1999; 122:17. [12] Yarnykh VL. MRM2012; 68:166. [13] Mossahebi P. et al. MRM2013. [14] Mossahebi ISMRM2012;4267 [15] Anderson A.et al. MRM2012 [16] Johnson K. et al. MRM2013, 70:1241. [17] Yarnykh VL. MRM2007; 57:192. [18] <http://medphysics.wisc.edu/~samsonov/qmap> [19] <http://surfer.nmr.mgh.harvard.edu>.

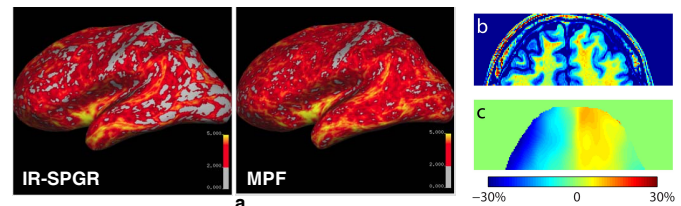


Figure 1. a: Cortical thickness estimated from IR-SPGR and MPF (both 1 mm³). IR-SPGR underestimates the thickness in areas of reduced WM/GM contrast arising due to B_1 field variations typical for high field MRI. Note increased spatial uniformity of cortical thickness measured with the quantitative myelin-sensitive MPF. The B1 effect is illustrated in (b, c). Reduced IR-SPGR WM/GM contrast in the right hemisphere (b) corresponds to the areas of elevated B_1 (c).

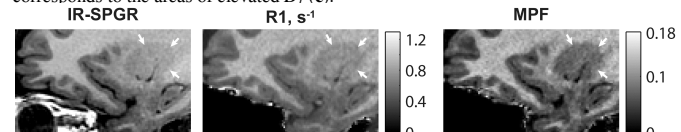


Figure 2. Improved visualization of deep GM structures on high resolution, myelin-sensitive MPF compared to the resolution-matched quantitative R_1 and inhomogeneity corrected anatomical IR-SPGR maps (arrows).

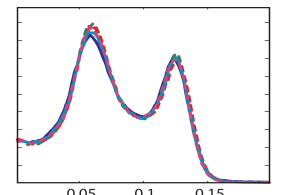


Figure 3. Whole-brain histograms of MPF obtained by 3p-mCRI protocol in an MS subject during 5 monthly visits.

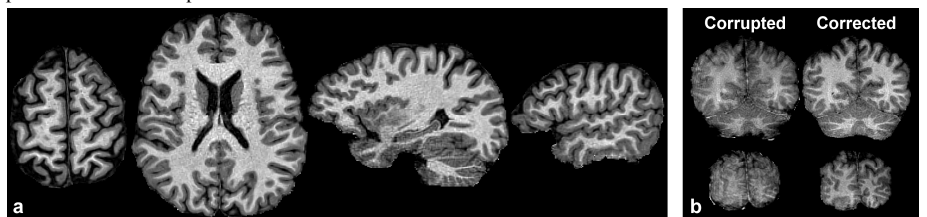


Figure 4. Results of MPF mapping with 3D undersampled radials at 1x1x1 mm resolution. a: MPF from non-corrupted dataset (two axial and two sagittal slices are shown). b: MPF from motion-corrupted dataset before and after motion correction (two coronal slices are shown; motion caused by intentional head movement of the healthy volunteer). Note significant improvement in tissue conspicuity in motion-corrected MPF.

ACKNOWLEDGEMENTS:

This work was supported by NIH (R01NS065034) and U.S. Dept. of Defense Congressionally Directed Medical Research Program (ASF).

Rapid and Accurate Variable Flip Angle T1 Mapping with Correction of On-Resonance MT Effects

Pouria Mossahebi¹, and Alexey A. Samsonov²

¹Biomedical Engineering, University of Wisconsin, Madison, WI, United States, ²Radiology, University of Wisconsin Madison, Madison, WI, United States

INTRODUCTION: Variable flip angle (VFA) acquisition using spoiled gradient echo (SPGR) [1] has become a widely accepted approach for fast high resolution mapping of longitudinal relaxation rate $R1=1/T1$. Recent studies have shown that magnetization transfer (MT) between free and bound protons due to the application of an on-resonance excitation pulses causes a significant bias in steady state MR signal in tissues with natural abundance of macromolecular content [2]. Ou et al predict up to 14% error in white matter (WM) VFA $T1$ values [3], an effect comparable to white matter $T1$ changes observed in multiple sclerosis [4]. Explicit consideration of a two-pool MT model in VFA experiments may improve the accuracy of $T1$ estimation [3]. However, due to very low sensitivity of the modified VFA signal model to parameters of the two pool MT model such as bound pool fraction (f), cross-relaxation rate (k), transverse relaxation times of the bound pool $T2^B$, and free pool $T2^F$, the feasibility of MT-corrected *in vivo* $T1$ mapping using VFA measurements only is limited. Cross-relaxation imaging (CRI) provides a convenient framework to model the effect of both off-resonance MT and on-resonance excitation pulses on bound and free proton pools [5]. It was recently demonstrated that combination of VFA and pulsed MT SPGR measurements within modified CRI framework may be used to remove bias due to on-resonance MT in both VFA $R1$ values and two-pool MT parameters [6]. However, this approach requires augmenting VFA measurements with multiple MT acquisitions to allow estimation of the full set of parameters. Here, we propose a method to obtain accurate $T1$ maps of clinical quality using a standard VFA datasets augmented with a single off-resonance MT SPGR scan (VFA-MT).

METHODS: The simultaneous fit of SPGR data (VFA part) and off-resonance MT SPGR (MT part) data to the modified CRI equation accurately yields all parameters of the model ($PD, R1, f, k, T2^B$) [6]. To achieve fast $T1$ mapping, we simplify the full model by setting $T2^B$, $T2^F R1^F$, and $R=k(1-f)/f$ to constrained values as proposed in [7] ($11\mu s$, 0.022 , and $19s^{-1}$, respectively), which leaves only three free parameters ($PD, R1, f$) for estimation. These parameters may be in principle determined using only three measurements (two VFA and one MT). The accuracy of this simplified 3-parameters/3-measurements approach (VFA-MT) was studied in simulations, phantom imaging, and *in vivo*. **Simulations:** We run simulations to identify the ranges of an offset frequency and an MT flip angle of a VFA-augmenting MT scan for which the effect of such constraints on accuracy of $R1$ and f is minimal. **Phantom Studies:** Phantom (25% gelatin) and *in vivo* experiments were run on a 3.0T GE MR750 (Waukesha, WI), and flip angle and field maps for all data were measured by an optimized AFI method [7] and IDEAL [8], respectively. Phantom protocol included acquisition of 3D VFA data $FAs=[7,15,35,50]^\circ$ and MT SPGR data ($FA=15^\circ$, $\Delta=2.5,5,9,13kHz$, $\alpha_{MT}=[850,1300]^\circ$, 18ms Fermi pulse, $120\times120\times88mm$ FOV, $128\times128\times44$ matrix, $TR/TE=37/2.3ms$). Single-slice, 2D inversion-prepared spin-echo (IR) data was collected to determine a reference $T1$ value in the phantom ($TR/TE=5000/8.2ms$, $TI=0.05,0.1,0.2,0.3,0.5,0.7,0.9,1.2,1.6,2s$). **In Vivo Studies:** Volunteer brain data included 3D VFA ($FAs=[5,10,20,30]^\circ$) and MT SPGR ($FA=10^\circ$, $\Delta=2.5,5,9,13kHz$, $\alpha_{MT}=[500,1100]^\circ$, 18ms Fermi pulse, $240\times180\times80mm$ FOV, $128\times96\times40$ matrix, $TR/TE=40/2.0ms$). The reference MT-corrected $T1$ maps were obtained by simultaneous fit of all VFA and MT data to the modified CRI model [6]. All processing was done by in-house nonlinear optimization routines.

RESULTS AND DISCUSSION: **Simulations:** Figure 1 illustrates the effect of two-pool MT model parameters on observable $T1$ values when calculated using standard VFA method. The error in $T1$ increases almost linearly with f for typical values of k observed in neural tissues (>1) and hence is expected to be most biased in macromolecular-rich tissues such as white matter. The sensitivity of $T1$ to $T2^B$ was negligible. Figure 2 shows the effect of off-resonance frequency and MT flip angle of a VFA-augmenting MT scan on the average loss in $R1$ and f for the proposed simultaneous constrained estimation of these parameters. Similar to observations in [7], there is a range of Δ and MT flip angle with low sensitivity to the fixed parameters ($\Delta=4-6kHz$, $\alpha_{MT}=400-600^\circ$). Therefore, the optimized set of measurements (SPGR $\alpha=[5,30]^\circ$; $\Delta=5kHz$, $\alpha_{MT}=500^\circ$) were used for *in vivo* validation of the constrained model. **Phantom Studies:** The proposed method was applied to correct $T1$ mapping in the phantom ($f\approx4\%$). Examination of mean phantom $T1$ values obtained with full CRI (12 measurements), proposed constrained VFA-MT (3 measurements) and VFA (2 measurements) confirmed that both full CRI and VFA-MT provide excellent agreement with the reference IR $T1$ measurement (Fig. 3). At the same time, VFA $T1$ was biased by approximately 9%, which is consistent with simulations in Fig. 1. **In Vivo Studies:** Images in Fig. 4 reveal that there is a visible bias in $T1$ map obtained with regular VFA compared to $T1$ maps obtained with on-resonance MT effect correction. The MT-corrected values ($T1_{WM}=1050\pm25$, $T1_{GM}=1537\pm25$) agree well with literature [10] ($T1_{WM}=1060$, $T1_{GM}=1630$), while VFA underestimated them ($T1_{WM}=931\pm34$, $T1_{GM}=1462\pm28$). The whole brain $T1$ histograms (Fig. 5) show excellent correlation between reference full CRI values and proposed VFA-MT approach. The method corrected VFA $T1$ values by 11.5% in WM and 6.2% in GM, which agrees well with the bias predicted by [3]. Analysis of ROI $T1$ measurements (Table 2) demonstrated excellent preservation of $T1$ mapping accuracy in both WM and GM (error<1%) when moving from full CRI (12 measurements) to constrained VFA-MT (three measurements) estimation. The errors in f maps (not shown here) were more significant but always <10%, which is consistent with results in [7].

CONCLUSIONS: Accurate estimation of $T1$ values from VFA measurements requires consideration of MT effects, which may introduce $T1$ bias roughly proportional to the macromolecular content. The fast $T1$ correction protocol developed in this work (VFA-MT) requires a single MT scan in addition to regular VFA measurements for accurate $T1$ mapping. The presented approach is promising for fast high-resolution whole brain $T1$ mapping within clinically acceptable scan times.

REFERENCES: [1] Deoni SC. et al. MRM 2003; 49:515. [2] Bieri O. et al. MRM 2006; 56:1067. [3] Ou X. et al. MRM 2008; 59:835. [4] Vrenken H. et al. Radiology 2006; 240:811. [5] Yarnykh VL. et al. Neuroimage 2004; 23:409. [6] Mossahebi P, et al, submitted to ISMRM 2012. [7] Yarnykh VL. ISMRM 2011, p.19. [8] Yarnykh VL. MRM 2007; 57:192. [9] Reeder SB. et al. MRM 2005; 54:636. [10] Deoni SC. JMRI 2007; 26:1106.

ACKNOWLEDGEMENTS:

The work was supported by NIH grant R01NS065034

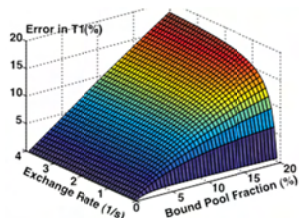


Fig. 1: Error of VFA $T1$ values vs. quantitative MT parameters f and k .

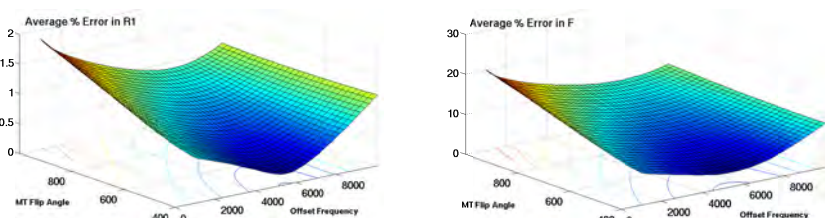


Fig. 2: Dependence of error in estimation of $R1=1/T1$ (left) and f (right) due to constraining vs. offset frequency and MT flip angle of a MT SPGR acquisition of proposed 3-point protocol.

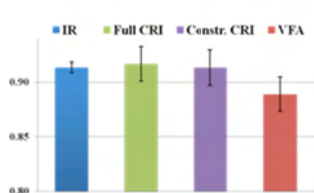


Fig. 3: Phantom $T1$ values calculated by different methods.

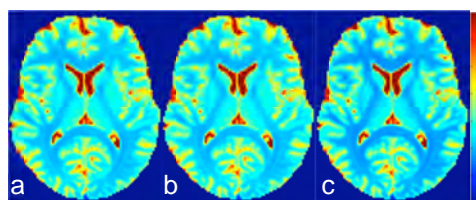


Fig. 4: *In vivo* $T1$ maps estimated by modified full (a) and constrained CRI (b), and VFA (c).

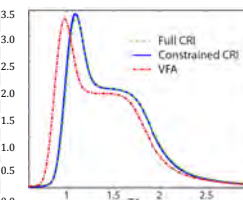


Fig. 5: Brain $T1$ histograms

	CC	IC	PT	CN
$T1$	0.77%	0.73%	0.45%	0.43%
f	3.05%	5.89%	4.22%	9.73%

Table 1: Errors of constrained method in brain structures (CC: Corpus Callosum, IC: Internal Capsule, PT: Putamen, CN: Caudate Nucleus)